

Controlling dynamic stall using vortex generators on a wind turbine airfoil

De Tavernier, D.; Ferreira, C.; Viré, A.; LeBlanc, B.; Bernardy, S.

DOI

[10.1016/j.renene.2021.03.019](https://doi.org/10.1016/j.renene.2021.03.019)

Publication date

2021

Document Version

Final published version

Published in

Renewable Energy

Citation (APA)

De Tavernier, D., Ferreira, C., Viré, A., LeBlanc, B., & Bernardy, S. (2021). Controlling dynamic stall using vortex generators on a wind turbine airfoil. *Renewable Energy*, 172, 1194-1211. <https://doi.org/10.1016/j.renene.2021.03.019>

Important note

To cite this publication, please use the final published version (if applicable). Please check the document version above.

Copyright

Other than for strictly personal use, it is not permitted to download, forward or distribute the text or part of it, without the consent of the author(s) and/or copyright holder(s), unless the work is under an open content license such as Creative Commons.

Takedown policy

Please contact us and provide details if you believe this document breaches copyrights. We will remove access to the work immediately and investigate your claim.



Controlling dynamic stall using vortex generators on a wind turbine airfoil

D. De Tavernier*, C. Ferreira, A. Viré, B. LeBlanc, S. Bernardy

Delft University of Technology, Kluyverweg 1, 2629HS, Delft, the Netherlands

ARTICLE INFO

Article history:

Received 6 November 2020

Received in revised form

3 March 2021

Accepted 4 March 2021

Available online 26 March 2021

Keywords:

Dynamic stall

Experiment

Vortex generators

Wind turbines

Vertical-axis wind turbines

ABSTRACT

Vortex generators (VGs) have proven their capabilities in wind turbine applications to delay stall in steady flow conditions. However, their behaviour in unsteady conditions is insufficiently understood. This paper presents an experimental study that demonstrates the effect of VGs in unsteady flow, including controlling and suppressing the dynamic stall process. An airfoil, particularly designed for a vertical-axis wind turbine, has been tested in a wind tunnel in steady flow and unsteady flow caused by a sinusoidal pitching motion. The steady and unsteady pressure distributions, lift, drag and moment were measured for a range of cases. The cases vary in motion (mean angle of attack, frequency, amplitude) and VG configuration. VGs have shown to delay or even suppress dynamic stall depending on the VG configuration, with particularly important factors being VG height and VG mounting position. The VGs promote a later dynamic stall onset and reduce the hysteresis loop. As soon as the VG's effectiveness vanishes, the configurations with VGs show a severe loss in normal coefficient, larger than in the case of the clear airfoil. However, the flow reattaches quicker and the airfoil recovers easier from the deep-stall conditions. The experimental results demonstrate that the use of VGs significantly changes the unsteady aerodynamic loads. This experimental database can serve for validation purposes to evaluate whether current modelling strategies in unsteady conditions are sufficient for blades equipped with VGs.

© 2021 The Author(s). Published by Elsevier Ltd. This is an open access article under the CC BY license (<http://creativecommons.org/licenses/by/4.0/>).

1. Introduction

Vortex generators are widely adopted in wind energy applications. On modern horizontal-axis wind turbines, they are usually applied inboard for stall separation control but also more outboard to improve predictability and increase the energy extraction [1]. Although VGs are simple, passive devices, the technical issues associated with the design and modelling of these blade add-ons are convoluted. The physics behind airfoils equipped with VGs is well studied in steady conditions. However, considering unsteady flow conditions in the design phase is becoming increasingly important, largely driven by the increasing size of wind turbines.

Blade-vortex interaction, yaw misalignment, wind shear and/or aero-elastic behaviour, among others, will cause dynamic, unsteady conditions to occur more frequently for large wind turbines, even in outboard regions of the blades [2–6]. In these cases, the blade airfoil will experience a time-dependent change in the boundary conditions at its surface due to, for example, pitching, plunging or

any other type of motion, or other interactions with the flow. Although it is often still possible to define an (equivalent) angle of attack, the loading differs significantly from the steady flow situation. While it is possible to define an angle of attack in steady conditions for which trailing edge separation, leading edge separation and stall occur, these phenomena tend to be delayed in the unsteady cycle. This change in the process of airfoil separation-stall-reattachment in unsteady flow is commonly called dynamic stall [5]. For vertical-axis wind turbines (VAWTs), this phenomenon is even more significant, due to the inherent unsteadiness of VAWTs [7–9]. The angle of attack of a VAWT is constantly changing. At low tip speed ratios (below 4), the angle of attack might exceed the static stall angle during rotation. As such, the dynamic effects are by definition an important aspect in VAWT aerodynamics [10–14]. For wind turbines, dynamic stall is considered the primary source of unsteadiness in the blade loads and as such has a significant effect on the performance and fatigue life of wind turbines. It may negatively affect power output, introduce excessive structural vibrations, thereby reducing the fatigue life of a turbine, or produce unwanted noise. Because of the rapid variations in the wind perceived by the blades, dynamic stall is also more

* Corresponding author.

E-mail address: d.a.m.detavernier@tudelft.nl (D. De Tavernier).

unpredictable in the case of wind turbines as opposed to, for example, helicopter rotors [15].

As the wind energy industry is anticipating extremely large wind turbines with long and flexible blades, it becomes crucial to evaluate and understand the performance and role of vortex generators, not only in steady conditions, but also in unsteady conditions. This may reveal that current modelling and design strategies are insufficient. Therefore, it is important to study how VGs behave in unsteady conditions and how do they affect the dynamic stall process. Specifically, the role of VGs in controlling and suppressing dynamic stall within the context of wind turbine blades should be studied. For these applications, the control objective is to reduce the lift overshoot due to the formation of the dynamic stall vortex but also to reduce the lift drop as the separation zone extends into the flow [15].

1.1. State-of-the-art

Dynamic stall onset is characterized by a phase where viscous effects cause a delayed separation of the boundary layer of the airfoil. Light dynamic stall is initiated by initial boundary-layer separation. The most obvious characteristic of dynamic stall is the vortex-shedding process preceding this separation. Often, the boundary-layer separation starts at the trailing edge, moving upwind with increasing perturbation. When the flow separation reaches the leading-edge (we will ignore cases of leading edge separation and reattachment), a leading edge vortex might be formed, which rolls up and convects downstream. This results in an extra lift component and moves the centre of pressure backwards. As soon as the separation zone grows to a size in the order of one chord, the flow becomes fully separated and the airfoil enters a state of deep stall [16–18]. At this moment, there is an overall loss of lift and an increase in drag, which is far more severe than in steady state conditions. The vortex reaches the trailing edge, detaches from the airfoil and moves into the wake. When reducing the angle of attack, the flow reattaches from front to rear and the aerodynamic loads return to the pre-stalled value. While dynamic stall is a significant, unsteady flow phenomenon beyond the static stall condition, unsteady effects will continue to affect the airfoil in attached flow. In both attached and separated flow, an amplitude damping/amplification and phase shift can be identified when compared with steady conditions. Several authors tend to refer to the phenomenon in attached flow as the Theodorsen effect [19].

The use of vortex generators (VGs) has extensively been investigated as a mean to suppress separation in steady conditions at a fixed angle of attack. Vortex generators create streamwise vortices from the free tips of the VGs (and at the wall according to Helmholtz theorem). These vortices enhance mixing between the high-energy flow in the outer part of the boundary layer with the low-energy regions near the walls, and re-energize the flow close to the surface. This makes the boundary layer more resistant against flow separation [20]. Studies by, for example, Baldacchino et al. [21,22] investigated the influence of VG parameters on airfoil performance of a DU97W300 wind turbine airfoil. These authors concluded that the chordwise position of the VGs and the VG height are of prime importance for the effectiveness of suppressing stall, while the VG length, inclination angle, shape, and array packing density are of secondary importance.

While the detailed performance of vortex generators in unsteady conditions is still largely unexplored, some efforts at uncovering the underlying mechanisms have been made. Most researchers have focused on vortex generators (in the broad meaning of the term) close to the leading edge. Martin et al. [23] demonstrated the use of counter-rotating rectangular VGs in a dynamically oscillating airfoil test. For the VR7 airfoil operating at a Mach number up to 0.3, the use of VGs installed at 10% of the chord

eliminated the pitching moment associated with dynamic stall completely in light stall cases, but failed for deep stall. Geissler et al. [24] also presented an experimental (and numerical) study focusing on the effect of miniature leading edge vortex generators on the OA209 airfoil section. Heine et al. [25] presented an experimental study in which the effect of passive low-aspect ratio cylinders mounted near the leading edge of an airfoil were studied in dynamic stall conditions. These cylinders serve as passive turbulence generators, and the experiments showed the effectiveness of these devices in reducing the negative pitching moment peak and hysteresis effects. While most researchers focus on passive VGs, Pape et al. [26] studied an active control principle based on deployable leading-edge vortex generators. Their paper addresses the validation of the effectiveness of the devices to delay static stall and alleviate dynamic stall penalties.

In wind turbine applications, VGs are typically positioned between 20% and 40% of the chord to balance the stall delay with the additional drag introduced by the VGs in pre-stall conditions. Zhu et al. [27] presented a numerical study of passive triangular VG positions between 20% and 40% of the chord on a wind turbine airfoil (DU97W300) in sinusoidally pitching conditions. The airfoil flow was simulated by numerically solving the unsteady Reynolds-averaged Navier-Stokes equations with fully resolved VGs. These authors concluded that the VGs were effectively suppressing the dynamic stall and that the lift hysteresis intensity is greatly reduced. The VG size and chordwise positioning proved to be of great importance to the effectiveness. The same authors [28] also presented the effect of a double-row of passive VGs as dynamic stall control device. This study was performed using unsteady RANS simulations on the NREL S809 airfoil with and without rectangular VGs. According to the authors, no experimental evidence is presented in literature for these kind of VGs in dynamic conditions.

In addition to vortex generators, several other means have been proposed in literature to control dynamic stall (particularly for wind turbine applications), including constant blowing air jets [29,30], periodic suction/blowing [31–34], leading edge suction [35], or plasma actuators [36–39].

1.2. Objective

For wind turbine applications, VGs are often positioned between 20 and 40% of the chord in order to balance stall delay and drag increase in pre-stalled conditions. Many studies have been performed to evaluate VGs in steady conditions. However, there is a lag in understanding the behaviour in unsteady conditions. Therefore, this work aims to *evaluate the role of VGs in unsteady conditions and experimentally demonstrate the use of VGs to control dynamic stall, with a particular interest towards wind turbine applications*. The goal of this paper is to report the experimental results that can guide further investigations in revealing the physical mechanism of VGs in dynamic conditions and consequently serve as a basis for validation purposes of dynamic stall modelling including VGs.

In this work, an experimental campaign is set up in the low speed, low turbulence tunnel of the TU Delft. Pressure measurements are taken in the wake and on the airfoil surface to identify the behaviour of an airfoil designed for a VAWT application. The effect on the lift, drag and moment coefficient of two VG sizes at different chordwise locations is studied statically. Furthermore, the airfoil is subjected to a sinusoidally pitching motion with various frequencies and amplitudes in the attached regime and in the positive and negative deep stall regimes. The effect of VGs on the unsteady behaviour is quantified and further investigated to identify the role of passive VGs in unsteady airfoil aerodynamics.

2. Methodology

2.1. Wind tunnel facility

An experiment is conducted in the low speed low turbulence wind tunnel (LTT) of Delft University of Technology [40]. The LTT is an atmospheric wind tunnel of the closed-throat single-return type. It is driven by a six-bladed fan with a 708 kW DC motor. The wind tunnel has an octagonal test section with a width of 1.80m, a height of 1.25m and a length of 2.60m. Its powerful motor allows to reach a maximum test section velocity of 100 m/s. The maximum chord-based Reynolds number for 2D airfoil testing, that can be achieved with acceptable blockage effects, is $3.5E6$. The wind tunnel can provide low levels of turbulence due to its high contraction ratio of 17.8 between the settling chamber and the test section. The free-stream turbulence level in the test section varies from 0.015% at 20 m/s to 0.07% at 75 m/s.

2.2. Wind tunnel model

The experimental test set-up consists of three main components i.e. the airfoil model, the pitching mechanism and the vortex generators. An artistic impression of these components is provided in Fig. 1.

The airfoil model tested in the wind tunnel has an airfoil profile specifically designed for a sub-megawatt scale vertical-axis wind turbine (VAWT) as part of the Tulyp Wind project under the RVO grant reference TEHE117057 [42]. The airfoil optimisation scheme is set up to balance the aerodynamic and structural performance. The aerodynamic objective at rotor scale is to maximize the power output. On airfoil scale, this is translated to maximize the lift gradient over drag in the angle of attack range that is encountered by the rotor. The structural objective function focusses on maximising the bending stiffness in flapwise direction. The work of Ferreira et al. [43–45] and De Tavernier et al. [46] presents more details of the airfoil optimisation scheme.

The airfoil profile, visualised in Fig. 2(a), has a maximum thickness of 25.48% chord and a trailing edge thickness of 1.36% chord. The airfoil coordinates are provided in Table A.2. The model had a chord length of $c = 0.36\text{m}$ and spans the height of the test section. This makes the model aspect ratio to be approximately 3.5. The airfoil model has been manufactured in 5 pieces using the Ultimaker S5 3D printer. The pieces are assembled together and stiffened with a steel non-circular rod in spanwise direction at the quarter chord point. Additionally, two extra end caps are manufactured from aluminium to avoid rotation of the rod inside the model. This is illustrated in Fig. 1(c). The blade surface is smoothed with sandpaper, inequalities are filled with spray filler and the surface is finished with spray paint. The centre piece of the model is equipped with 75 pressure orifices with a diameter of 0.4 mm surrounding the airfoil model. The pressure taps are installed under an angle such that they do not interfere with each other.

The thermal images in Fig. 2(b-c) displays the pressure and suction side of the airfoil at zero angle of attack $\alpha = 0^\circ$ and Reynolds number $RE = 1E6$. The transition from the light to the dark color represents the location of transition from laminar to turbulent flow. These results are used to confirm the mostly 2D behaviour of the flow. Note, however, that a small dark peak is present on the pressure side, indicating that at that spanwise location, early transition occurs due to the presence of unwanted roughness. This location is assumed to be far enough (in the order of a chord length) from the location of the pressure orifices and the impact on pressure measurements is deemed to be sufficiently small. Also, the sensitivity to this roughness element is not visible for all angles of attack. It depends on the location of natural transition as well as the boundary layer thickness. A thinner boundary layer (occurring at smaller angles of attack) is more sensitive to the roughness element than a thicker boundary layer.

In some cases, transition is forced at 5% chord length measured from the leading edge both on the suction and pressure side. This is realised by using zig-zag tape. The zig-zag tape has a thickness of 0.2 mm.

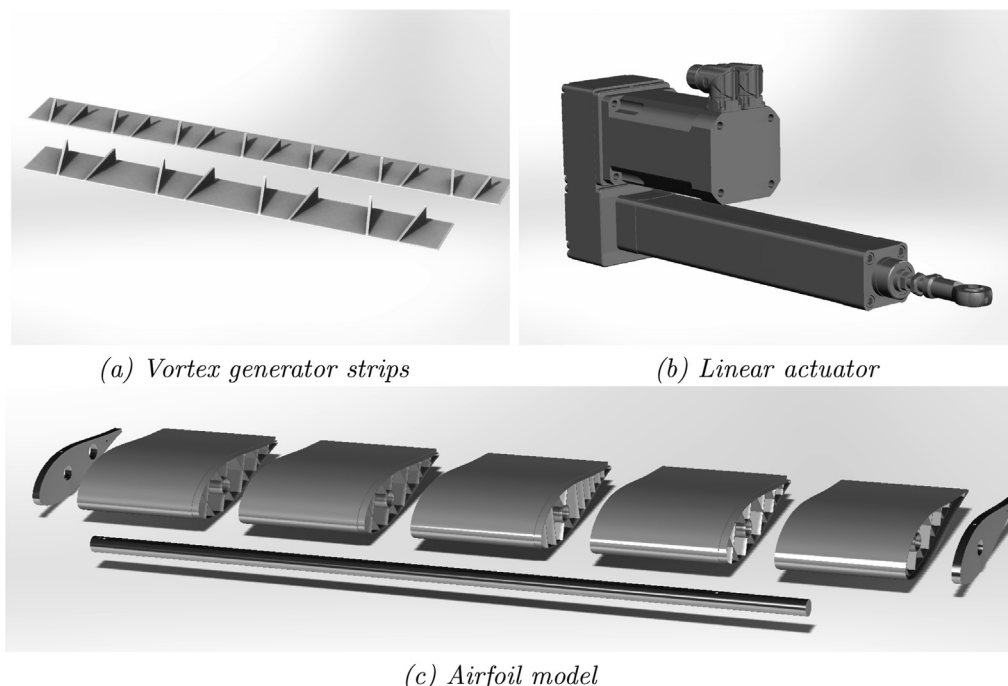
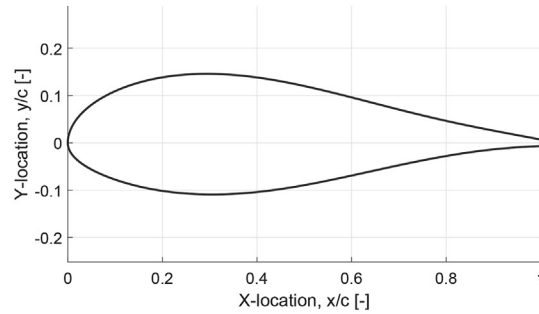


Fig. 1. CAD-drawings of the components used in the test set-up [41].



(a) Cross-section of the DU17DBD25 airfoil

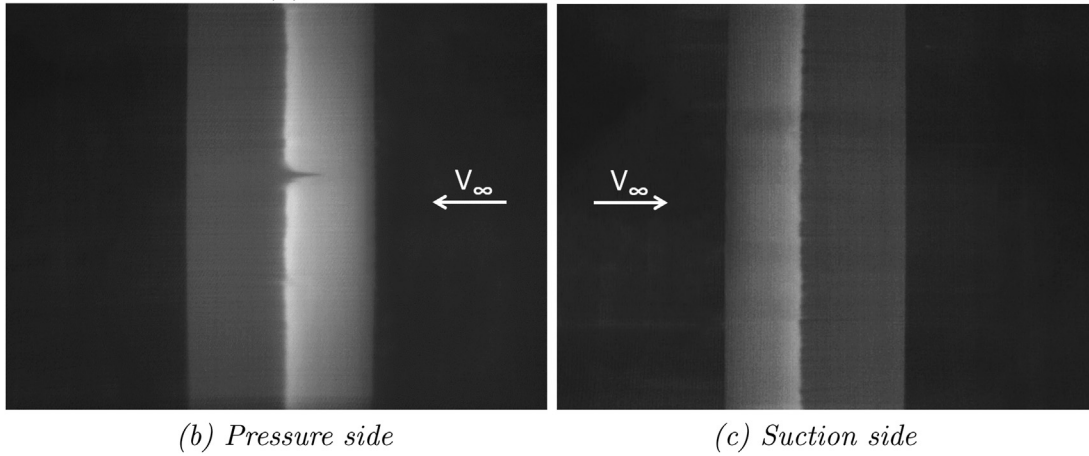


Fig. 2. Thermal images of pressure and suction side of the DU17DBD25 airfoil at an angle of attack of 0° and a Reynolds number of 1E6.

The airfoil model is equipped with vortex generators along its span. The VGs are sized and designed based on the results of the experimental parametric study performed by Baldacchino et al. [22]. Delta-shaped vortex generators are designed, spaced in counter-rotating configuration. Two sizes are considered, where VG1 is the largest with a height of $h_{VG} = 6\text{mm}$, a length of $l_{VG} = 18\text{mm}$ and an inflow angle of $\beta = 15^\circ$. The inter-vane distance d_{VG} is 21 mm while the inter-pair distance D_{VG} is 42 mm VG2 is smaller and has a height of $h_{VG} = 4\text{mm}$. All other dimensions are scaled with respect to the VG height. The VG height is sized with respect to the boundary layer thickness calculated by Xfoil [47] near the stall angle at $x/c = 0.3$. For easy handling and installation of the VGs on the airfoil surface, the individual vanes are attached to a strip with an approximate length of 200 mm, 20 mm width and 0.5 mm thickness, as shown Fig. 1(a). The sizing variables are visualised in Fig. 3. The VGs are manufactured using 3D printing.

For the static polar tests, the airfoil blade is clamped vertically in between the walls of the tunnel. A turning table is used to rotate the blade and change the static angle of attack. For the dynamic test, in

which the airfoil is subjected to a pitching motion, the steel rod inside the model is connected to a linear actuator. The linear actuator uses a crank mechanism to rotate the blade at relatively high frequencies. The blade is clamped and set in place using rotating bearings at the top and bottom. To avoid friction between the tunnel walls and the model, a small gap of 1 mm at each side is allowed. For the static tests, this gap is taped, while for the dynamic test the gap remains open. The outlet of the pressure tubes going through the model requires a hole in the bottom wall. We note that this could cause unavoidable 3D effects in the unsteady polars. Fig. 1(b) shows the commercially available off-the-shelf electric cylinder actuator with a precision ball screw drive used in the experiment. The actuator is controlled using LabVIEW.

In Fig. A.18 in the appendix, some additional pictures are provided from the experimental set-up. It includes photos of a piece of the 3D printed model, including pressure tabs, the finished assembled model, the model installed in the test section and the pitching mechanism installed on top of the wind tunnel.

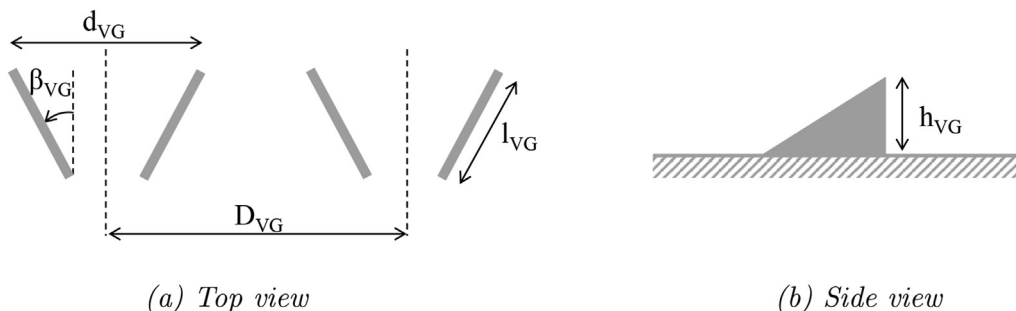


Fig. 3. Top and side view of the VG configuration. All VG size variables are indicated.

2.3. Data acquisition and post-processing

The pressure measurements performed on the airfoil surface and in the wake allow to determine the 2D lift and drag of the model. The wake rake, positioned behind the airfoil, measures the static and the total pressure in the wake. It has 67 total pressure tubes and 16 static pressure tubes over a length of 504 mm. The pressure deficit between the pressure in the wake and in the free stream, or essentially the momentum loss of the flow, is directly related to the profile drag. The uncorrected drag is obtained using Equation (1). $C_{p,t}$ and $C_{p,s}$ are the total and static pressure in the wake. Integrating the pressure coefficient of the upper ($C_{p,u}$) and the lower surface ($C_{p,l}$) allows to determine the normal force coefficient of the blade (see Equation (2)). From the normal force and the drag force, the lift coefficient can be determined as given by Equation (3), in which α refers to the angle of attack. The moment coefficient around the leading edge is defined as Equation 4

$$C'_d = \frac{2}{c} \int_{wake} \sqrt{C_{p,t} - C_{p,s}} (1 - \sqrt{C_{p,t}}) dy \quad (1)$$

$$C'_n = \int_0^1 (C_{p,l} - C_{p,u}) d\left(\frac{x}{c}\right) \quad (2)$$

$$C'_l = \frac{C'_n}{\cos(\alpha)} - C'_d \cdot \tan(\alpha) \quad (3)$$

$$C'_{m,LE} = \int_0^1 \left[C_{p,u} \left(x + \frac{dy_u}{dx} y_u \right) - C_{p,l} \left(x + \frac{dy_l}{dx} y_l \right) \right] d\left(\frac{x}{c}\right) \quad (4)$$

The measured lift, drag and angle of attack are corrected using the standard corrections for wall effects as given by Allen and Vincenti [48]. This includes lift-interference, wake blockage, solid model blockage and streamline curvature. When the wake becomes unstable or wider than the wake rake, it is impossible to retrieve the drag from the wake rake. In that case the drag is derived from the surface pressure, which is common practice. Data is gathered at 5Hz and averaged over approximately 25 s. During this time period, the wake rake is moved up or down in spanwise direction. Pressure ports that are covered with VGs or zig-zag tape are disregarded from the calculations. For the steady measurements, thermal cameras were also installed to monitor the pressure and suction side of the airfoil model. These thermal images provide information about the location of transition, separation (to some extent) and 3D variations.

To retrieve the force coefficients for the dynamically pitching airfoil, the pressure measurements need to be corrected. The signal received at the transducer carries a phase lag and attenuation compared to the signal at the surface of the airfoil. To correct for this, the software tool PreMeSys V2.0 [49] (Pressure Measurement System version 2.0) is used. This tool translates the Bergh and Tijdemans theory from 1965 [50] into an easy user-friendly Matlab code. The response time is obtained by subjecting the system to small amplitude perturbations. The theory assumes that the system is a series connection of N pressure tubes where the output pressure of a particular tube is the input pressure of the next tube. The transfer function between the pressure at the port opening and the pressure sensed by the pressure sensor (for a single pressure measuring system) is given by Bergh and Tijdeman [50], as given in Equation (5). A series of connecting tubes is nothing more than the combination of all pressure relationships within its path from the

first to the last volume/tube, as given in Equation (6).

$$\frac{p_1}{p_0} = \left[\cosh(\phi L) + \frac{V_v}{V_t} \left(\sigma + \frac{1}{k} \right) n \phi L \sinh(\phi L) \right]^{-1} \quad (5)$$

$$\frac{p_N}{p_0} = \frac{p_N}{p_{N-1}} \frac{p_{N-1}}{p_{N-2}} \dots \frac{p_1}{p_0} \quad (6)$$

where $\phi = \frac{\nu}{a_0} \sqrt{\frac{j_0(\alpha)}{j_2(\alpha)}} \sqrt{\frac{\gamma}{n}}$ with $\alpha = \frac{3}{i^2} R \sqrt{\frac{\rho_s \nu}{\mu}}$ is the shear wave number including viscosity, i is the imaginary unit, ρ_s is the mean density, ν is the frequency, μ is the absolute fluid viscosity, $n = \left[1 + \frac{\gamma-1}{\gamma} \sqrt{\frac{j_2(\alpha) \sqrt{Pr}}{j_0(\alpha) \sqrt{Pr}}} \right]^{-1}$ is the polytropic constant, $Pr = \frac{\mu C_p}{\lambda}$ is the Prandtl number, $\gamma = \frac{C_p}{C_v}$ is the specific heat ratio, J_m is the Bessel function of the first kind with order m , σ is the dimensionless increase in transducer volume due to diaphragm deflection, k is the polytropic constant for the volumes. The three geometrical parameters which affect the frequency response function are the tube radius R , the tube length L and the pressure transducer and tube volume V_v and V_t [50]. The possibility of an oscillating air column inside the pressure tubes due to the airfoil motion is not considered as an additional factor for the reliability of pressure measurements.

While this theory is extensively validated in literature by comparing the experimental and theoretical results of the phase-lag and amplification for various measuring systems with different tube lengths and tube radii [50], we have set up a simple calibration test to demonstrate the correct use of this model and its implementation in this particular application. A random pressure signal is applied to a tube. The signal is split in two and the response is measured at the beginning of the tube and at the end of the tube. The tube is a replica of the tube used in the real experimental set-up from the pressure port at the airfoil surface till the pressure measurement system. A schematic representation as well as a photo of this calibration test is provided in Fig. 4. The result of two independent calibration tests is presented in Fig. 5, although more tests are performed. The green line represents the signal measured at the end of the tube. The blue line is the pressure signal measured at the beginning of the tube and serves as the reference. The red, dashed line shows the signal at the end of the tube corrected with the Bergh and Tijdemans theory. Various frequencies and amplitudes are applied. The error between the reference signal and the corrected signal is nearly normally distributed with a mean of 0.49Pa and a standard deviation of 40.40Pa. This calibration test demonstrates a correct implementation of the theory to this application.

After correcting the pressure signals for the phase delay and amplitude loss, the pressure at the airfoil surface can be translated to the normal load coefficient and moment coefficient around the leading edge as given in Equation (2) and Equation (4) respectively. The drag cannot be calculated, meaning that the lift coefficient can also not be retrieved. For every unsteady angle of attack variation, data is taken for at least 20 revolutions at a sampling frequency of 300Hz. Pressure ports that are covered by zig-zag tape or VGs are disregarded from the calculations. Additionally, pressure ports that visually showed a clear response delay compared to the other ports are not further considered.

2.4. Test plan

Experimental data is acquired for a predefined set of test cases. This set of test cases is summarised in Table 1. The data set consists of a set of steady polars in free and forced transition (using zz-tape at 5%) state, with and without VGs. The angle of attack ranges from

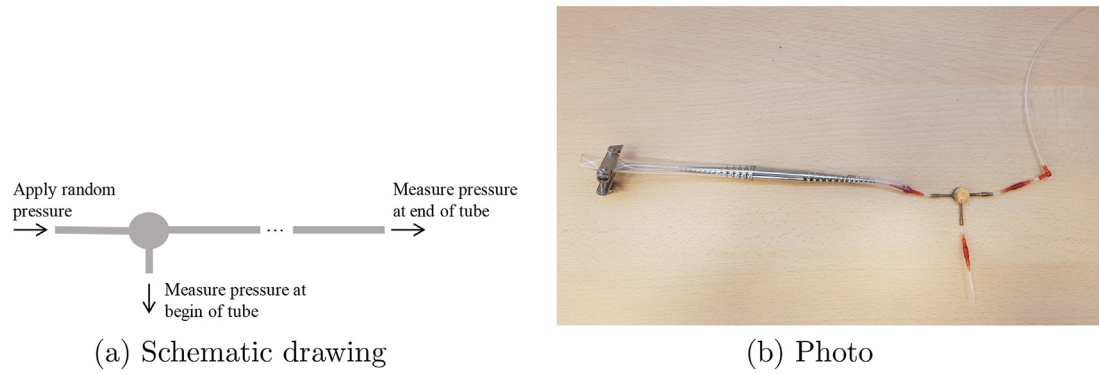


Fig. 4. The set-up of a calibration test to validate the Bergh and Tijdeman's theory to correct for the unsteady signal measured at the end of the tube compared to the real signal at the beginning of the tube.

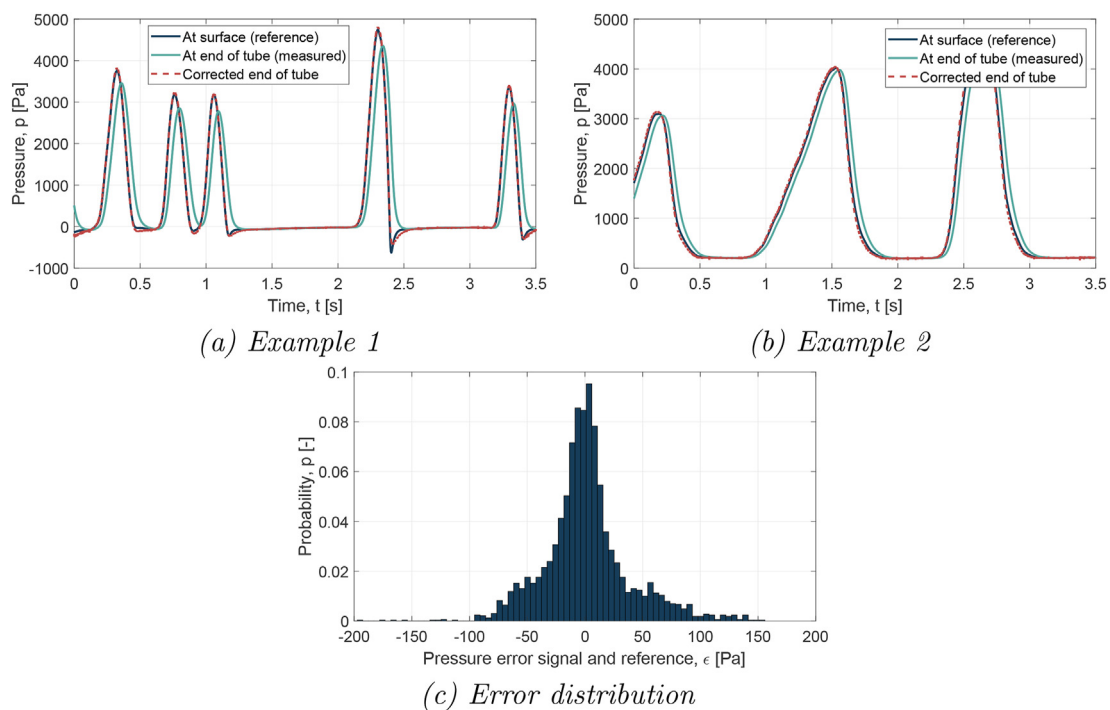


Fig. 5. Validation of unsteady pressure signal correction method using the Bergh and Tijdeman's theory.

around -25° to 25° , to make sure that the stall region is captured properly. For the steady cases, no frequency is defined. An unsteady data set is gathered for a sinusoidally varying angle of attack. The angle of attack oscillations are defined by a mean angle of attack a_0 , an amplitude A and a frequency f , and given by Equation (7). t is the time in seconds.

$$\alpha(t) = a_0 + A \cdot \sin(2\pi ft) \tag{7}$$

The unsteady polars are similarly collected in free and forced transition state, with and without VGs. Depending on the airfoil configuration, the mean angle of attack is set between $a_0 = -15^\circ$ and 15° and the amplitude from $A = 3^\circ$ to 7° . The frequency is varied from $f = 0.5$ to 2Hz , which corresponds to a reduced frequency of $k = 0.014$ to 0.054 . The reduced frequency k is a dimensionless value defining the degree of unsteadiness at a certain frequency and is given by Equation (8). For values below 0.03 , the unsteady effects are generally small while the flow becomes highly unsteady for values above 0.03 . The Reynolds number

is kept constant at $RE = 1E6$. This corresponds to a wind speed of around 42 m/s . The turbulence level is well below 0.015% .

$$k = \frac{\pi cf}{V_\infty} \tag{8}$$

While not all cases will be used in the results and discussion of this work, the post-processed experimental data sets and some supplementary graphs are publicly available via the 4TU Centre for Research Data (see Ref. [51]).

3. Results & discussion

3.1. Steady polars

Before analysing the behaviour of the airfoil in unsteady conditions, it is important to quantify and understand the effect of the VGs on the static behaviour of the airfoil.

In Fig. 6, thermal images are presented of the airfoil's pressure

Table 1
Overview of the steady test cases (top) and unsteady test cases (bottom).

Reynolds no.	Transition	VGs	VG loc.	Mean AoA	Amplitude	Frequency	Reduced freq.
$Re [-]$	—	—	$x_{VG}/c [-]$	$\alpha_0 [^\circ]$	$A [-]$	$f [Hz]$	$k [-]$
Steady polars:							
1E6	Free	—	—	–25 to 25	0	0	0
		VG1	0.2	–25 to 25	0	0	0
		VG1	0.3	–25 to 25	0	0	0
		VG1	0.4	–25 to 25	0	0	0
		VG2	0.2	–25 to 25	0	0	0
		VG2	0.3	–25 to 25	0	0	0
1E6	Forced	—	—	–25 to 25	0	0	0
		VG1	0.2	–25 to 25	0	0	0
		VG1	0.3	–25 to 25	0	0	0
		VG1	0.4	–25 to 25	0	0	0
		VG2	0.2	–25 to 25	0	0	0
		VG2	0.3	–25 to 25	0	0	0
Unsteady polars:							
1E6	Free	—	—	–15,-10,0,10,15	3,5,7	0.5,1,1.5,2	0.014,0.027,0.041,0.054
		VG1	0.2	–10, 0, 10	7	1,2	0.027,0.054
		VG1	0.3	–10, 0, 10	7	1,2	0.027,0.054
		VG1	0.4	–10, 0, 10	7	1,2	0.027,0.054
		VG2	0.2	–10, 0, 10	7	1,2	0.027,0.054
		VG2	0.3	–10, 0, 10	7	1,2	0.027,0.054
1E6	Forced	—	—	–15,-10,0,10,15	3,5,7	0.5,1,1.5,2	0.014,0.027,0.041,0.054
		VG1	0.2	–10, 0, 10	7	1,2	0.027,0.054
		VG1	0.3	–10, 0, 10	7	1,2	0.027,0.054
		VG1	0.4	–10, 0, 10	7	1,2	0.027,0.054
		VG2	0.2	–10, 0, 10	7	1,2	0.027,0.054
		VG2	0.3	–10, 0, 10	7	1,2	0.027,0.054
		VG2	0.4	–10, 0, 10	7	1,2	0.027,0.054

side with and without VGs at an angle of attack of 7° and a Reynolds number of 1E6. The incoming flow goes from right to left. In this example case, VGs with a height of 4 mm are installed at 40% of the chord on both sides of the airfoil. The thermal images reveal the effect of the VGs in a qualitative way. It is evident that the VGs (installed on a strip with 0.5 mm thickness) cause the flow to transition earlier. The shed vortices of the VGs and their downstream path can be recognised. In the absence of VGs, it is expected that the flow is mostly 2D and thus the spanwise variation should be negligible. VGs do introduce a three-dimensional flow; however, the flow becomes spanwise periodic because of the array configuration. To assess the airfoil drag coefficient with VGs from the wake rake, a spanwise traverse was conducted, spanning a range of three

VG pair spacings ($3 \times D_{VG}$). A typical wake scan as a function of the span is shown in Fig. 7 for an angle of attack of 0° and 6° . At the location of a VG pair, at the inflow region, the drag coefficient reaches its minimum. In this region, there is a strong downwash creating a fuller boundary-layer profile. In between two VG pairs, in the so-called upflow region, the flow is moved away from the wall causing an additional momentum deficit. Therefore, the drag coefficient is reaching a maximum value at that spanwise location. To assess the 2D drag coefficient, the spanwise average (ranging three VG pairs) is computed.

In Fig. 8 and Fig. 9, the (spanwise-averaged) lift and drag polars are provided of the clean airfoil as well as the airfoil equipped with VGs at different positions. In Fig. 8 the airfoil is exposed to a free

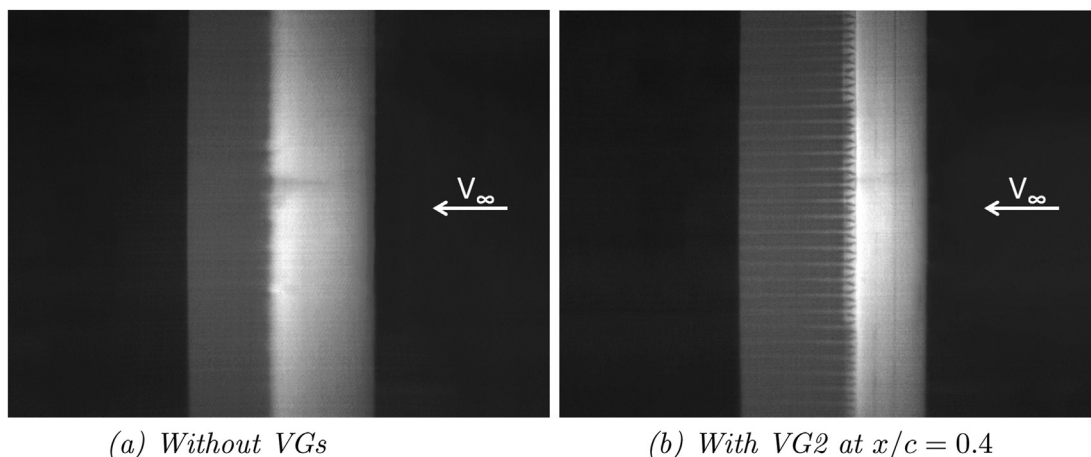


Fig. 6. Thermal images of pressure side of the airfoil with and without VGs at an angle of attack is 7° .

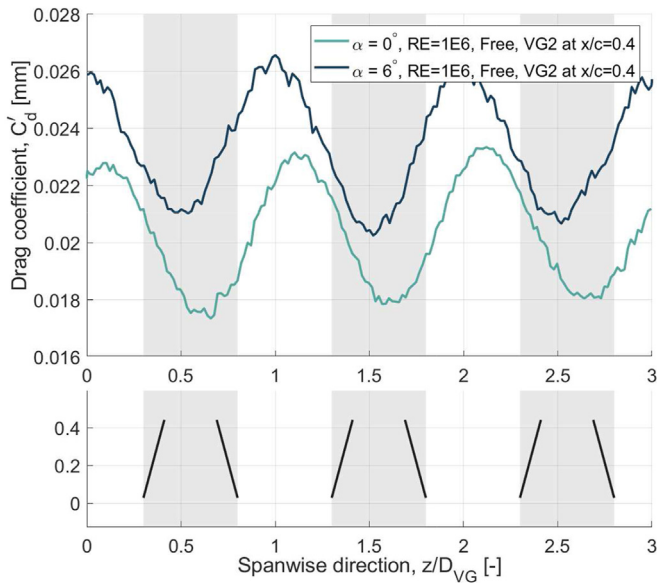


Fig. 7. Drag coefficient as a function of spanwise direction extracted from the wake-rake pressure data.

transition case while Fig. 9 considers the airfoil in forced transition conditions. Forced transition is created by means of zig-zag tape at 5% of the chord on the suction and pressure side.

The choice of VG height and chordwise positioning plays a significant role in the effectiveness of the VGs to delay static stall. In all flow conditions, the highest lift coefficient is experimentally achieved with the largest VGs at the most forward position that is considered in this experimental campaign. Also, the VGs positioned closest to the leading edge can postpone the stall angle the most and achieve a wider drag bucket. In general, the largest VGs

generate larger vortices, create more downwash, re-energize the boundary layer by convecting more momentum from the external flow into the near-wall flow and thus make the boundary layer more resistant to the adverse pressure gradient. This makes the boundary layer stronger to overcome separation. VGs positioned closer to the leading edge have a larger control space. Hence, for a larger range of angles of attack the streamwise vortices will be shed upstream the separation point. The lift slope in the linear part of the polar is increasing with VG size and is the smallest at the most forward mounting position. The lift polars show that the more forward the VG mounting position, the more abrupt the stall characteristic. The drag at zero lift shows a significant increase that may be attributed to the earlier transition (mainly depending on the VG location) on one hand and on the additional VG profile drag (mainly depending on the VG size) on the other hand. These observations apply to the polars in the positive and negative angles of attack region as well as in free and forced transition. In forced transition, stall occurs earlier and there is more drag at zero lift compared to the free transition case. In Fig. A.19 and Fig. A.20, the experimental lift and drag polars are compared to the polars calculated by XfoilVG [52].

More information on the flow around the airfoil can be gathered from the pressure distribution at the airfoil surface. In Fig. 10 and Fig. 11, the experimental pressure distributions are presented for the DU17DBD25 airfoil at an angle of attack in the linear part of the polar and one above stall in absence of VGs. For the free transition case, the selected angles of attack are $\alpha = 7^\circ$ and $\alpha = 20^\circ$. For the forced transition case, these angles are $\alpha = 5^\circ$ and 15° . Note that at the location of the VG and/or zig-zag tape, no pressure measurements are available and linear interpolation is performed.

At the smallest angle of attack, the pressure distributions are nearly identical for all VG configurations. These distributions imply that the flow is attached over the entire surface. In the pressure distribution of the large angle of attack, clear differences may be observed. Fig. 10(b) and (d) reveal that only VG1 at 20% and 30% or

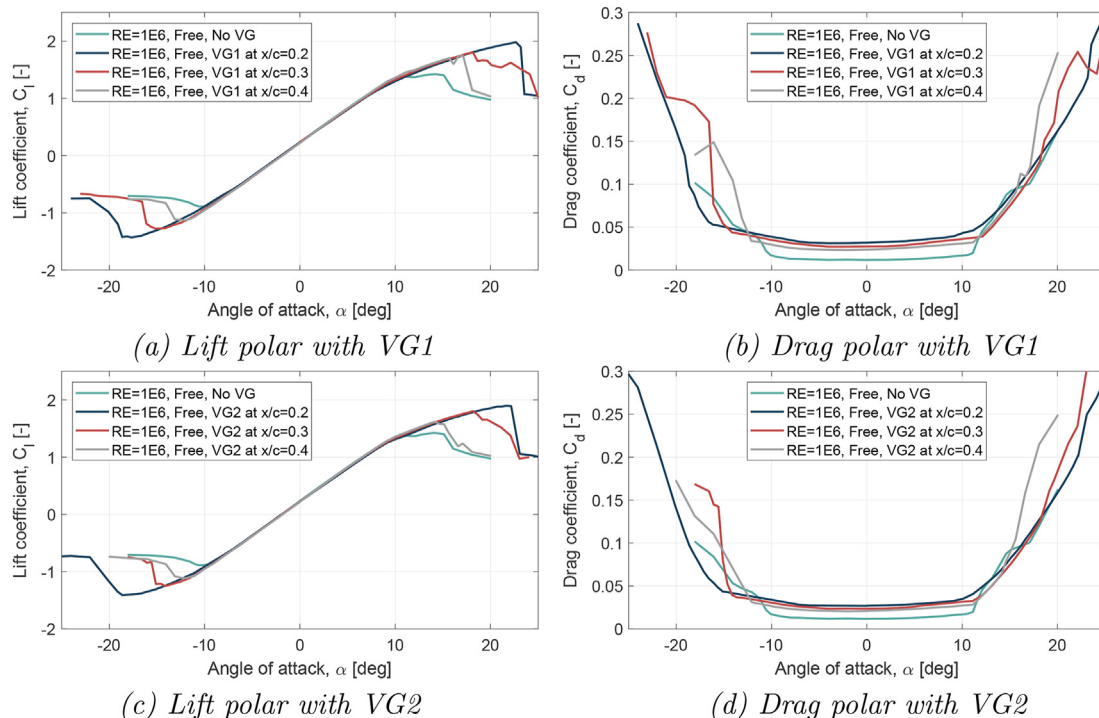


Fig. 8. Experimental lift and drag polar in free transition with various VG configurations.

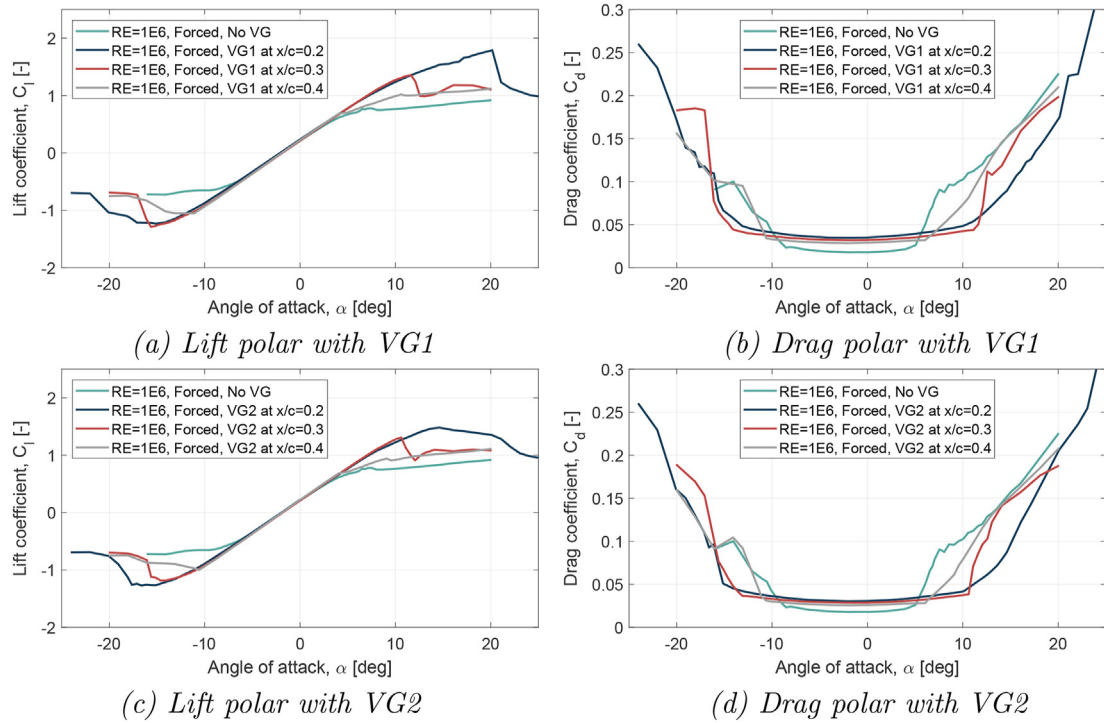


Fig. 9. Experimental lift and drag polar in forced transition with various VG configurations.

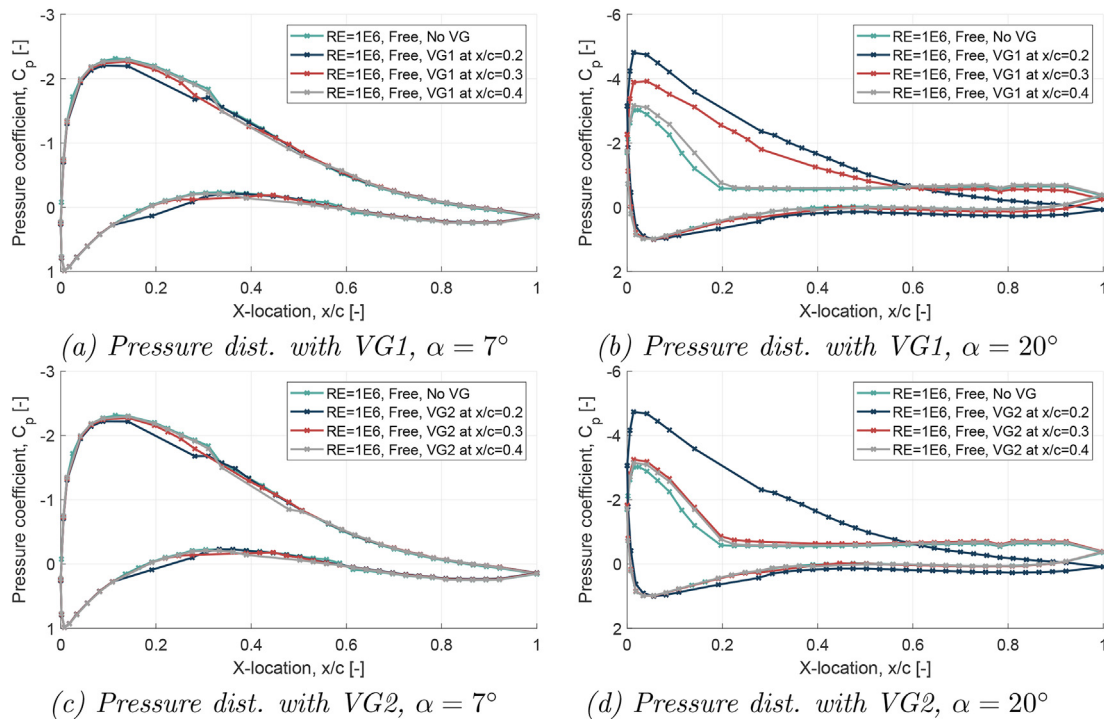


Fig. 10. Experimental pressure distribution in free transition with various VG configurations.

VG2 at 20% are able to prevent the airfoil from stalling in free transition. All other configurations show a clear stalled behaviour at this angle of attack. This is evidenced by the plateau of constant pressure initiated at $x/c = 0.2$ on the suction side. In case of forced transition, a similar observation can be made. In the linear part of the polar, the pressure distributions and thus the lift are rather

similar. At an angle of attack of 15° (see Fig. 11(b) and (d)) the airfoil without VGs is fully stalled and the flow is separated for nearly 70% of the airfoil. With VGs, the flow remains attached longer but the point of separation (if any) depends on the mounting point of the VGs. In forced transition, it is only the VGs installed at $x/c = 0.2$ that may keep the flow completely attached. In all other cases the flow

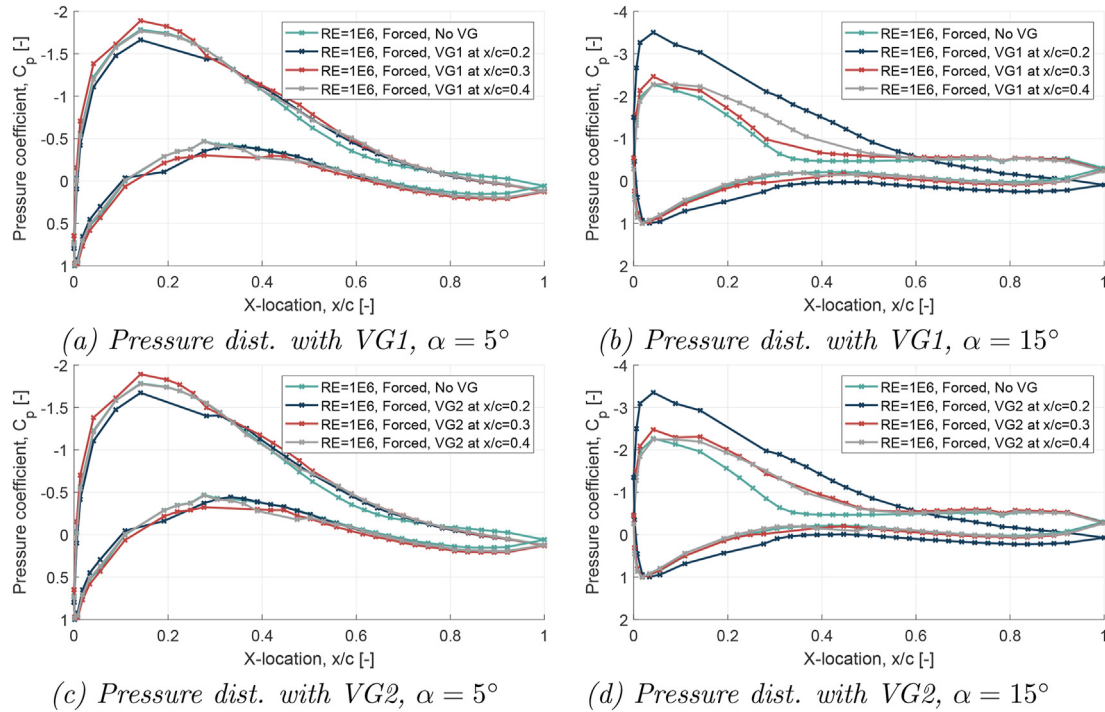


Fig. 11. Experimental pressure distribution in forced transition with various VG configurations.

separates but more downstream than in case of no VGs. From Fig. 11(b) it can be identified that the flow around the airfoil with VG1 at $x/c = 0.4$ remains attached longer than in case the same VGs are installed at $x/c = 0.3$. This is a clear example of the fact that VGs positioned more upstream may reach a larger stall angle but experience a more abrupt stall behaviour.

The observations made in the lift polar, drag polar and pressure distribution as a function of the VG height and positioning follow the conclusions made by Baldacchino et al. [22].

3.2. Unsteady polars without VGs

In Fig. 12 and Fig. 13, the aerodynamic response to a sinusoidally oscillating angle of attack is presented. Three pitching motions are considered: (1) $a_0 = -11^\circ, A = 7^\circ, f = 2\text{Hz}$, (2) $a_0 = -1^\circ, A = 7^\circ, f = 2\text{Hz}$ and (3) $a_0 = 9^\circ, A = 7^\circ, f = 2\text{Hz}$. The three cases represent unsteady conditions in the deep stall region of the negative angles of attack, in the linear part of the polar and in the deep stall region of the positive angles of attack respectively. The normal coefficient, moment coefficient and pressure distributions at $\alpha = a_0$ are analysed. In the figures, a distinction is made between the part of increasing angle of attack (upstroke, indicated with a full line) and the part of decreasing angle of attack (downstroke, indicated with a dashed line). The shaded area presents the standard deviation over 15 revolutions. The steady polars are also represented in the normal and moment polars.

The unsteady effects in attached flow cause a hysteresis loop. The variation of the normal and moment coefficients are lagging behind the change in angle of attack since the wake is not immediately updated and, thus, not fully developed. In the up-going stroke, the normal coefficient is lower than in steady case, while the moment coefficient (around the leading edge) is larger. In the down-going stroke, the opposite is true. The average slope of the normal coefficient polar is slightly lower than in steady case.

A larger unsteady effect is recognised in deep dynamic stall conditions. The unsteady curves are characterized by a higher

maximum normal coefficient, a higher stall angle, a large hysteresis loop and a larger (negative for positive angles of attack and positive for the negative angles of attack) peak pitching moment. The fluctuations (i.e. the standard deviation) of the curves during 15 revolutions is the largest in the downstroke and significantly larger in case of separated flow compared to attached flow.

The pressure distributions at the mean angle of attack ($\alpha = a_0$) in the upstroke and downstroke are not identical. The flow is mainly attached in the upstroke. On the other hand, in the downstroke, the flow is separated at the same angle of attack. In the attached flow region, the difference between up- and downstroke is significantly smaller.

In forced conditions, similar observations may be made. The stall behaviour in steady case is less abrupt in forced conditions than in clean conditions. This seems to affect the behaviour in unsteady conditions, as the hysteresis loop is smaller.

As already mentioned earlier, a small gap of 1 mm was present between the wind tunnel walls and the airfoil model. Additionally, there was a hole in the bottom wall to be able to connect the pressure ports of the model to the measurement system. In steady conditions these gaps were taped, while this was no longer possible in the unsteady measurements. This might introduce unwanted, yet unavoidable, 3D effects that are not present in the steady polars.

One of the parameters that dictates the unsteady behaviour of the airfoil model is the oscillation frequency f . The larger the frequency, the more unsteady the operating conditions are. In Fig. 14, the experimental normal coefficient polar is presented for four different frequencies, namely $f = 0.5\text{Hz}, 1\text{Hz}, 1.5\text{Hz}$ and 2Hz . For this experiment, this corresponds to a reduced frequency of $k = 0.014, 0.027, 0.041$ and 0.054 . The mean angle of attack is set to $a_0 = -1^\circ$ or 9° to present the effect of the oscillation frequency in attached and separated flow. The amplitude of the angle of attack oscillations are set to $A = 7^\circ$.

In attached flow, an increasing oscillation frequency causes the hysteresis loop to become wider. The difference between the up-going and down-going stroke is, thus, the largest for larger

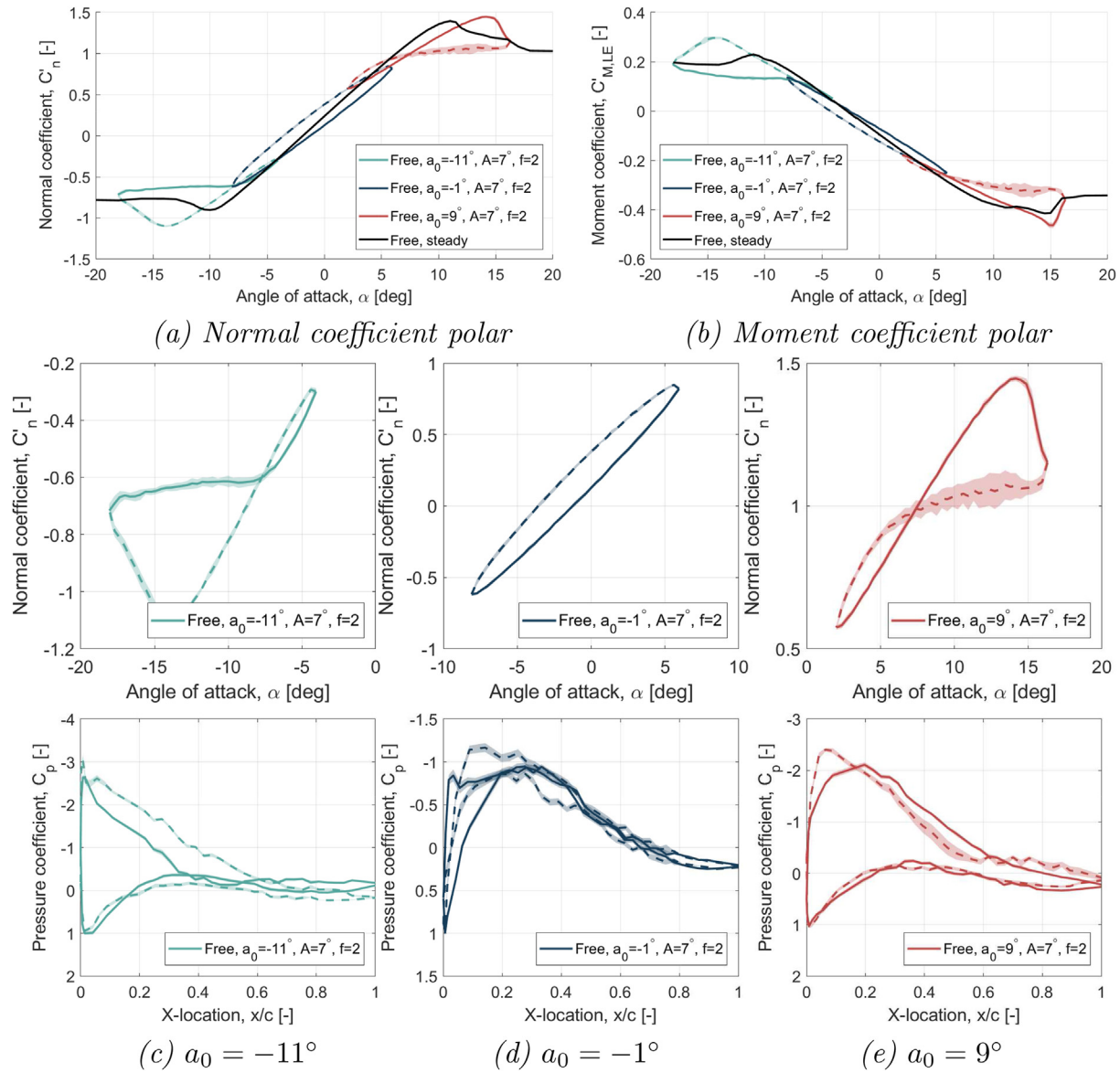


Fig. 12. Dynamic normal coefficient polar, moment coefficient polar around the leading edge and pressure distributions at $\alpha = a_0$ in free transition.

frequencies. At higher frequencies, the aerodynamic properties lag the angle of attack variations more. Also, the slope of the normal coefficient decreases with increasing frequency. In case of deep-stall conditions (see Fig. 14(b)), the hysteresis significantly increases with the oscillation frequencies and stall-induced drop in normal coefficient is larger. The maximum achieved normal coefficient and corresponding angle of attack is the largest for high frequencies but it also takes more time to reattach the flow again in the down-going stroke. This can be derived from the pressure distributions over the airfoil surface (not presented here). Also, the overall slope of the normal coefficient is reduced. The negative peak moment is the largest for the highest frequency.

Another parameter of interest is the oscillation amplitude A . The pitching rate is linearly proportional to the amplitude. From Fig. 15(a), one could argue that the width of the hysteresis (the difference between pitching up and pitching down) is the largest for higher amplitudes in case of attached flow. Fig. 15(b) shows the effect of the oscillation amplitude in separated conditions. Since a larger angle of attack is reached at larger amplitudes, a bigger part

of the airfoil separates and the size of the hysteresis loop increases. With an amplitude of $A = 3^\circ$, the flow separates only close to the trailing edge. The part of the flow more upstream remains attached. In case of an amplitude of $A = 7^\circ$, stall is delayed further than in case of $A = 5^\circ$, yet the hysteresis is larger and the recovery takes longer. The slope of the normal coefficient seems not to depend on the oscillation amplitude.

The observations with respect to the reduced frequency and oscillating frequency without flow control are in agreement with what is previously reported in older and more recent publications (for example Ref. [17,53–57]).

3.3. Unsteady polars with VGs

In this section, the influence of vortex generators on the dynamic stall characteristics is studied. In attached flow, the effect of VGs on the normal and moment coefficient is negligible. Therefore, the focus of this section is on medium- and deep-stalled conditions in the positive and negative angle of attack regime. The influence of

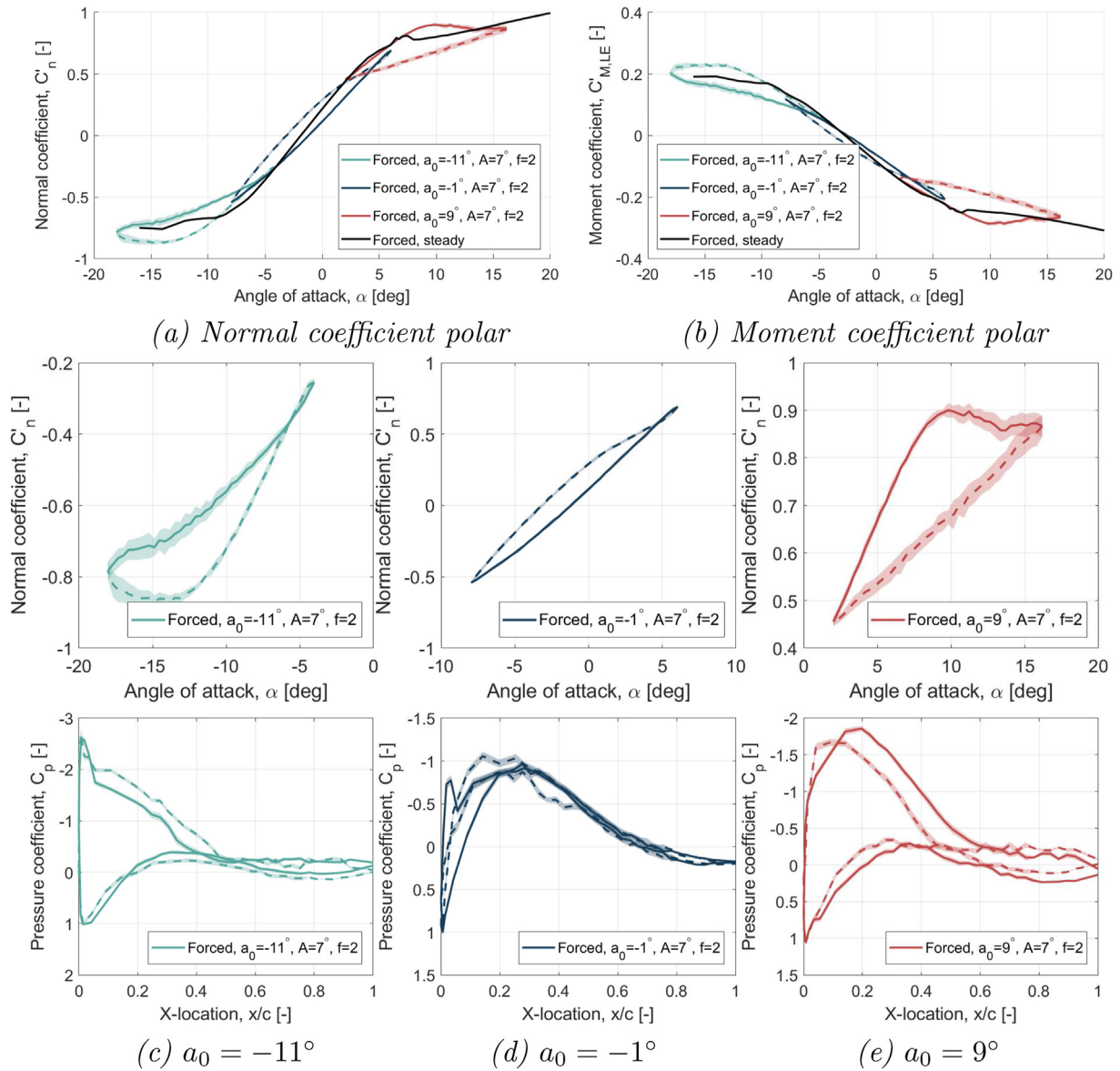


Fig. 13. Dynamic normal coefficient polar, moment coefficient polar around the leading edge and pressure distributions at $\alpha = a_0$ in forced transition.

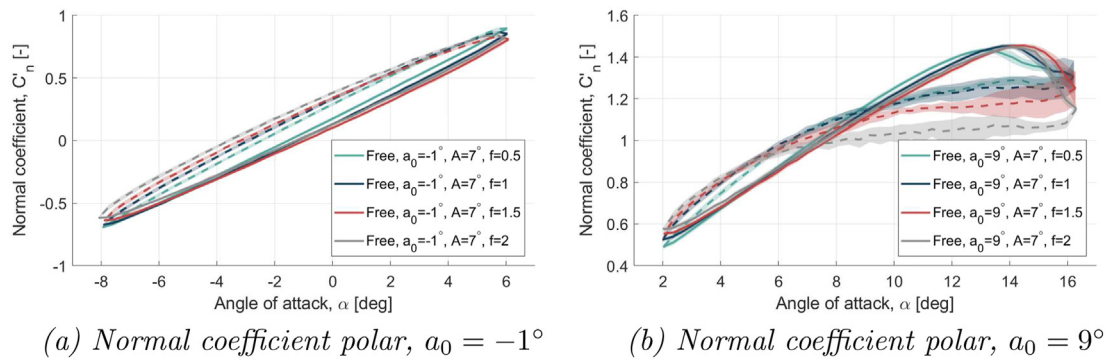


Fig. 14. Dynamic normal coefficient polar in free transition for various oscillating frequencies.

the VGs is analysed on the overshoot in normal coefficient, the dynamic stall onset, the size of the hysteresis loop and the process

of recovery and reattachment.

Fig. 16 presents the effect of the VG location on the dynamic stall

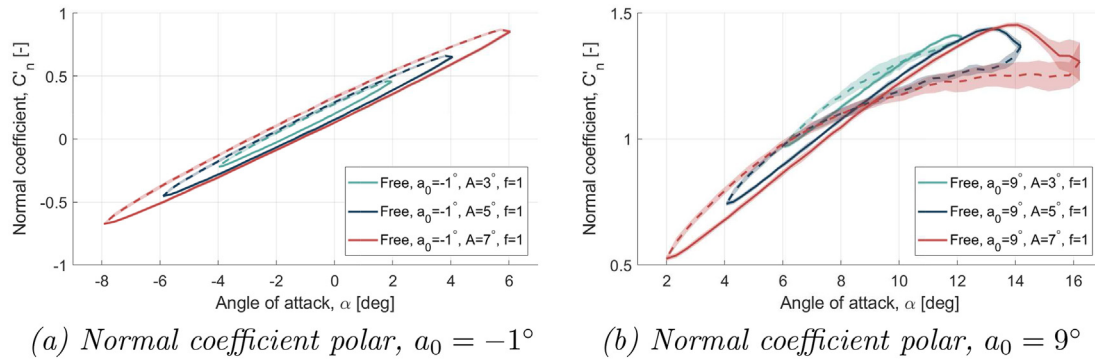


Fig. 15. Dynamic normal coefficient polar in free transition for various oscillating amplitudes.

behaviour. It contains the normal coefficient polar, the moment coefficient around the leading edge polar, the pressure distribution at $\alpha = a_0$ in the up-going stroke and the down-going stroke. The angle of attack is varied dynamically with an amplitude of 7° at a frequency of 2 Hz. This corresponds to a reduced frequency of 0.054 for this experimental set-up. The mean angle of attack is either $a_0 = 9^\circ$ or $a_0 = -11^\circ$ to be able to capture dynamic stall in the positive and negative angle of attack range respectively. The airfoil model is equipped with VG1 along its whole span at three locations: (1) $x/c = 0.2$, (2) $x/c = 0.3$ and $x/c = 0.4$. As a reference, the measurements of the clean airfoil without VGs are also presented.

Consider first the positive angle of attack range and the results presented in Fig. 16(a–c–e–g). The airfoil model with VGs (for all mounting positions), shows that the hysteresis loop in the normal and moment coefficient polars is significantly suppressed. A larger maximum normal coefficient is achieved and a higher peak moment is reached. The slope of the normal and moment coefficient polar is the largest when the VGs are installed at the most downstream position. This corresponds to the results in steady case. The pressure distribution at an angle of attack of $\alpha = 9^\circ$ in the up-going stroke does not show much dependency on the VG location. The flow is attached in absence of the VGs as well as with the VGs. However, at the same angle of attack in the down-going stroke, the presence of the VGs causes the flow to remain attached. Contrary, without VGs the flow is separated for nearly 50% of the airfoil.

In the negative angle of attack region, where $a_0 = -11^\circ$, more effect of the VG location may be observed. The aerodynamic results are given in Fig. 16(b–d–f–h). The normal and moment coefficient polars already reveal that only VG1 at 20% chordwise position is able to fully suppress dynamic stall and keep the flow attached. All other cases show a clear dynamic stall behaviour and a large hysteresis. This was expected, since the airfoil model with VG1 at 20% in steady-state conditions is the only one that is not stalling at $\alpha = -18^\circ$.

Since the airfoil with the VGs installed more downstream experiences deeper stall (i.e. a larger part of the flow is separated) at $\alpha = -18^\circ$, a larger hysteresis is expected, which is clearly visible in Fig. 16(b). With VGs, a higher maximum C_n is achieved. However, the drop in C_n as the flow separation moves upstream is more significant compared to the case without VGs. This could be interpreted to be different, as was indicated in the studies with VGs near the leading-edge [25,26].

As soon as the effectiveness of the VGs to overcome the high adverse pressure gradient reduces, the aerodynamic properties approach the results of the clean airfoil. The aerodynamic behaviour of the airfoil with VG1 installed at 30% remains in between the behaviour with VGs installed at 20% (fully attached) and with the

VGs installed at 40% (fully separated). The recovery of the deep stall occurs the fastest for the VGs installed most upstream. This observation can be supported by the pressure distributions at $\alpha = -11^\circ$ shown in Fig. 16(f) and (h), for the up-going stroke and down-going stroke respectively. In the down-going stroke (for decreasing angle of attack), all cases present very similar pressure distributions. For the up-going stroke, where the angle of attack is increasing again, it is clear that in case of the clean airfoil and the airfoil with VG1 at $x/c = 0.4$, the flow is separated from 35% on. As the VGs are installed in front of the separation point in clean airfoil case, the flow remains attached.

The size of the VGs already showed to affect the effectiveness of the VGs in steady conditions. As such, it might be possible to also identify an effect in unsteady conditions. In Fig. 17, the normal coefficient polar of the DU17DBD25 airfoil in forced transition conditions is presented. A distinction is made between VG1 and VG2 mounted at various chordwise locations along the span. The results are presented for a dynamically oscillating angle of attack where $A = 7^\circ$, $f = 1$ Hz and $a_0 = 9^\circ$ or $a_0 = -11^\circ$. By comparing Fig. 17(a–b) with Fig. 17(c–d), one may conclude that the airfoil model equipped with VG1 can suppress the dynamic stall hysteresis significantly more than VG2. VG1 is shedding stronger vortices, mixing the outer flow more with the inner flow and can, thus, prevent separation more than VG2. This is clearly visible in the size of the hysteresis loop, the deep stall angle and the recovery speed. It may be recognised both in the positive and the negative angle of attack range.

Although the purpose of this paper is not to reveal the physical reasons of the favourable effects of the VGs on the dynamic stall behaviour, it is reasonable to expect that the vortices developed by the VGs itself will interact with the boundary layer. The additional momentum transfer of the vortices created by the VGs will delay the stall onset, resulting in a delayed separation of the boundary layer and subsequent formation of the leading-edge vortex [15,28]. In the deep stall regime, where the leading-edge vortex dominates the flow field, the interaction of the VG's vortices may lead to a prolonged leading-edge vortex growth phase and, thus, a larger vortex. This could explain the increased normal force drop and pitching moment during detachment. The faster recovery may be attributed to the additional mixing and re-energising of the boundary layer due to the VGs. A detailed analysis of this interaction is recommended future investigations to confirm these thoughts.

4. Conclusion

This paper presents an experimental study of a wind turbine airfoil equipped with passive vortex generators undergoing pitch

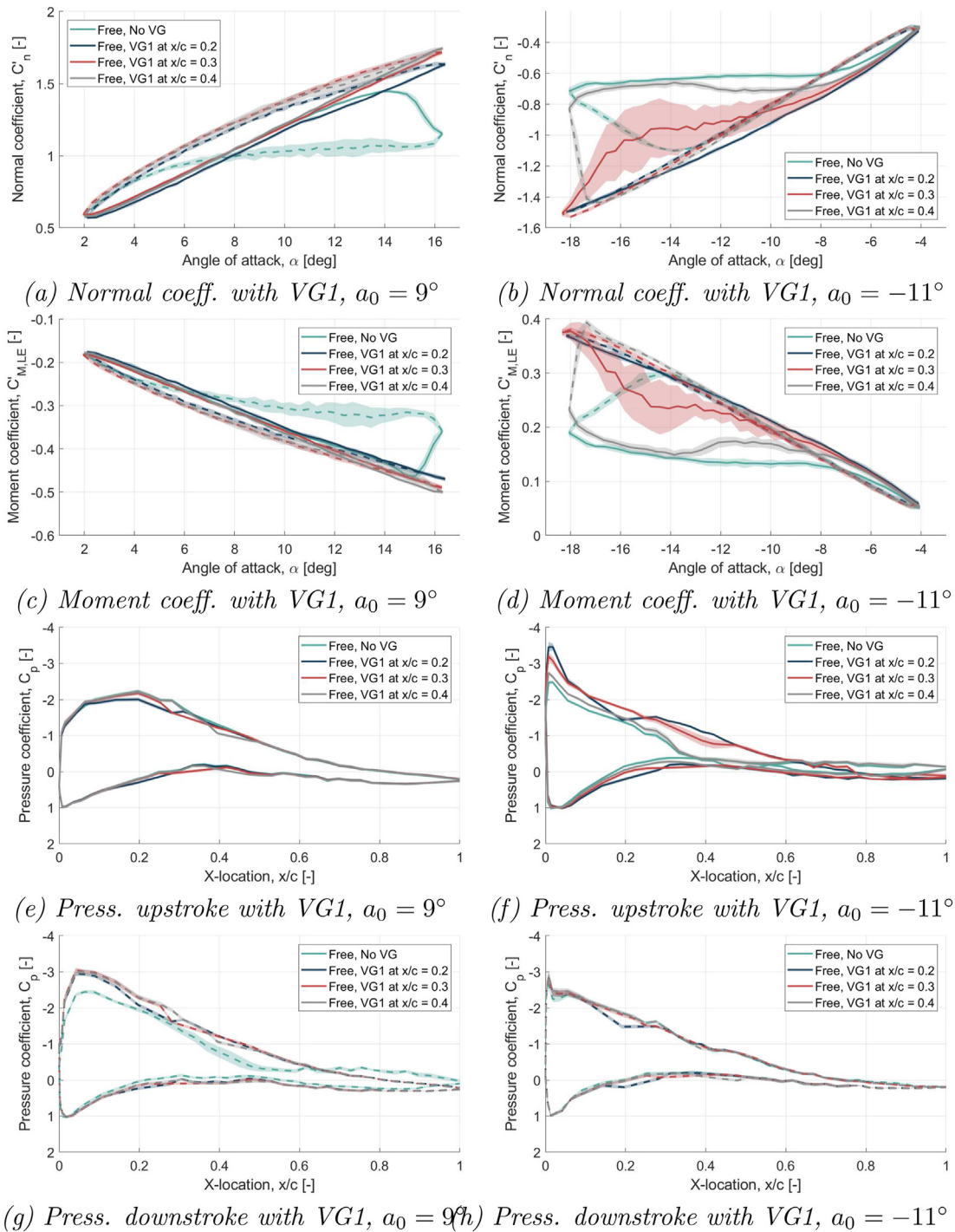


Fig. 16. Dynamic normal coefficient polar, moment coefficient polar and pressure distribution at $\alpha = a_0$ in free transition with various VG configurations.

oscillations. The unsteady behaviour of the aerodynamic properties is analysed, in order to identify the role of VGs in suppressing or preventing dynamic stall.

An experiment is set up in the low speed, low turbulence wind tunnel of the TU Delft. The model has a DU17DBD25 profile, which is specifically designed for a sub-MegaWatt vertical-axis wind turbine. The model is equipped with vortex generators of two different sizes (the VG height is sized with respect to the boundary layer thickness near the stall angle at $x/c = 0.3$) and mounted at different chordwise positions along the span. The aerodynamic

properties are analysed in free transition conditions and forced transition conditions by using zig-zag tape at $x/c = 0.05$ on pressure and suction side. Pressure measurements are taken on the airfoil surface and in the wake in steady and unsteady conditions.

The steady polars evidenced that the maximum lift coefficient and corresponding stall angle are the largest for the biggest VGs mounted at the most upstream position (VG1 at $x/c = 0.2$). The bigger VGs generate larger vortices, push more momentum from the external flow into the near-wall flow and thus make the boundary layer more resistant to the adverse pressure gradient that

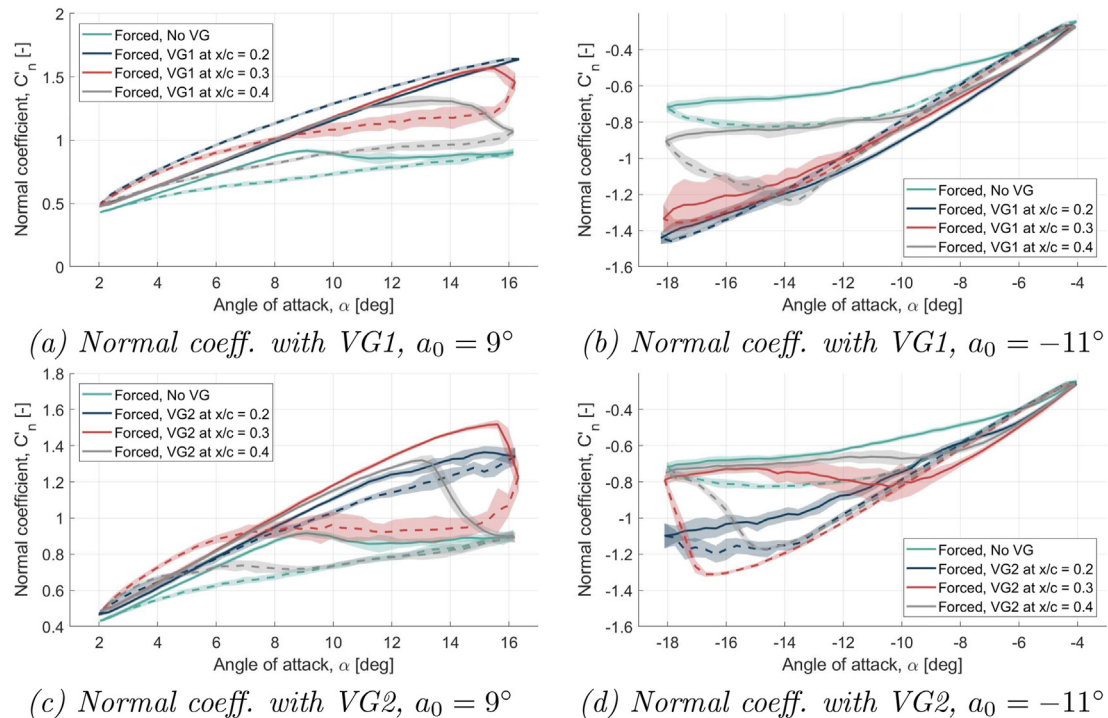


Fig. 17. Dynamic normal coefficient polar, moment coefficient polar and pressure distribution at $\alpha = a_0$ in forced transition with various VG configurations.

induces separation. The vortices shed by the VGs positioned closer to the leading edge, have a larger control space. The drag at zero lift increases in presence of the VGs due to the additional profile drag and earlier transition to turbulent flow.

The performance of the wind turbine airfoil in unsteady conditions showed that in attached flow, the hysteresis is small and remains close to the steady polar. The average lift slope decreases with increasing oscillating frequency. In medium-to deep-stall conditions, the hysteresis significantly increases with the oscillating frequencies. The normal coefficient overshoot and corresponding angle of attack is the largest for high frequencies, but it also takes more time to reattach the flow again in the down-going stroke. Introducing vortex generators enables the suppression of dynamic stall and delay the onset as long as the VGs can overcome the high adverse pressure gradient and prevent separation. Therefore, the VG mounting location and height play a significant role. However, as soon as the angle of attack becomes too large, the dynamic stall process is still initiated (and this depends on the VG configuration), the drop in normal coefficient is significantly more severe than in case of a clean airfoil. The VGs do help the flow to reattach quicker.

From this study, it may be concluded that the use of passive VGs in wind turbine applications is highly promising in controlling the unsteady aerodynamic loads. Although VGs introduce an extra drag component, they cause a later onset of dynamic stall. This implies that wind turbines would be able to withstand larger variations in wind speed and direction without entering dynamic stall conditions. Additionally, preventing or at least suppressing dynamic stall will reduce the load variations and, thus, improve the fatigue life.

This experimental database is of significant use in developing and calibrating unsteady models. It could be used to evaluate current modelling strategies and derive closure relations for VGs in unsteady flow for integral boundary-layer methods and/or CFD

methods. This work could also serve as a basis for revealing the physical reasons of the favourable effects of VGs on the dynamic stall behaviour. This development and understanding is crucial in order to model wind turbines in unsteady conditions and further quantify how VGs affect load variations and the wind turbine design.

Availability of data and material

The experimental data used in this study is made publicly available on: <https://doi.org/10.4121/13089581>.

CRediT authorship contribution statement

D. De Tavernier: Writing - original draft, Formal analysis. **C. Ferreira:** Writing - original draft, Formal analysis. **A. Viré:** Writing - original draft. **B. LeBlanc:** Writing - original draft, provided the airfoil shape. **S. Bernardy:** Writing - original draft.

Declaration of competing interest

The authors declare that they have no conflict of interest.

Acknowledgements

This work has been funded by the Tulyp wind project under the RVO grant TEHE117057, the Netherlands Enterprise Agency, under a Hernieuwbare Energie (Sustainable Energy) subsidy. The authors would like to thank Steve van Herk and Rein van den Oever for their advice in 3D printing the model and setting up the pitching mechanism.

Appendix A. Appendix

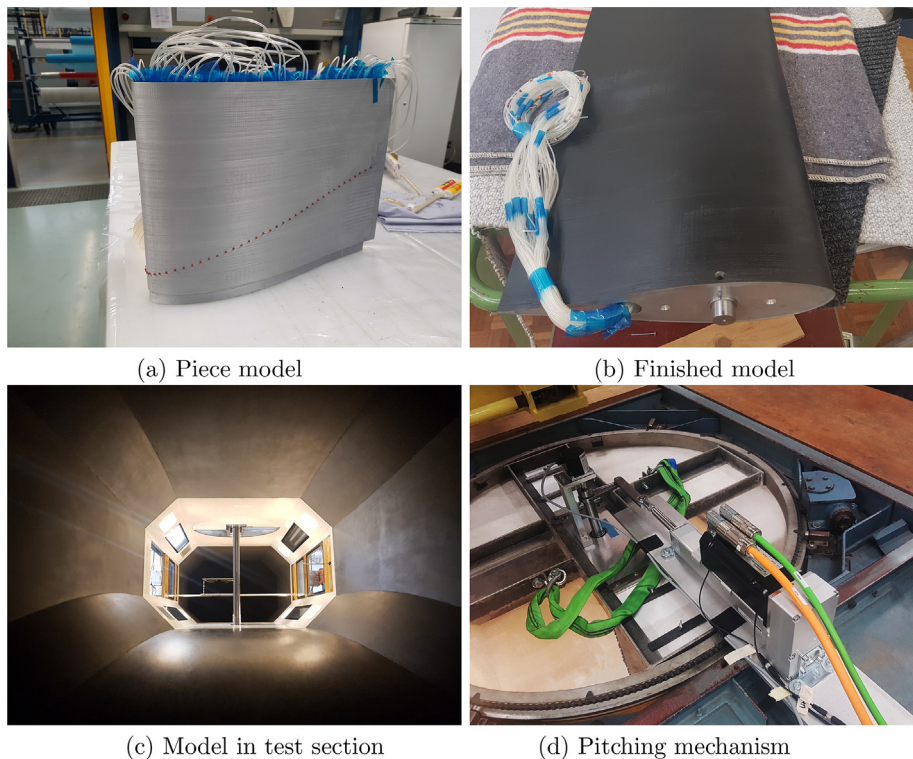


Figure A.18. Pictures of the experimental set-up and equipment.

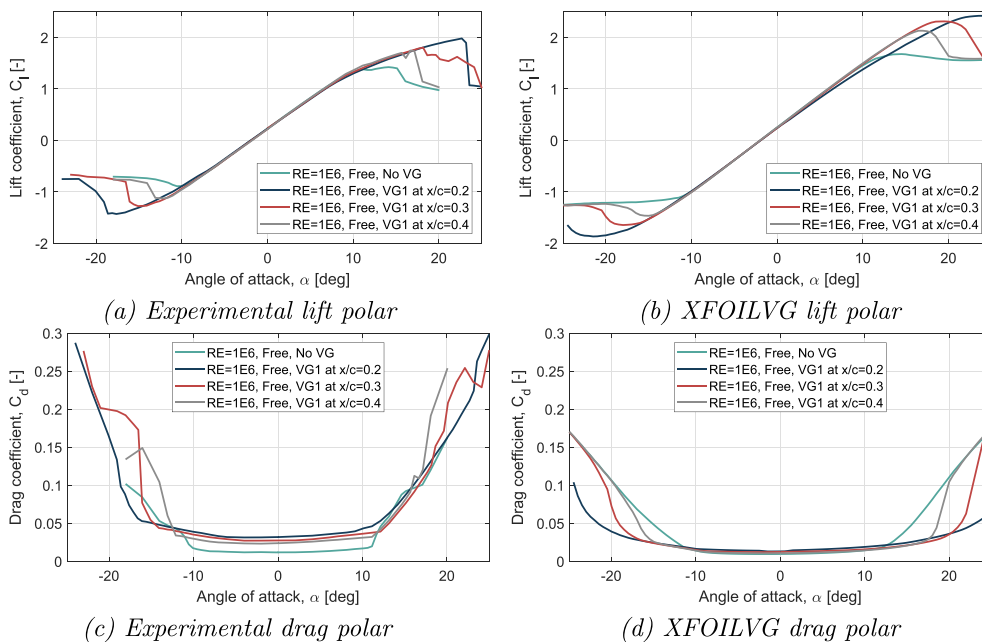


Figure A.19. Experimental lift and drag polar and polars obtained with XFOILVG [52] for DU17DBD25 in free transition with various VG1 configurations.

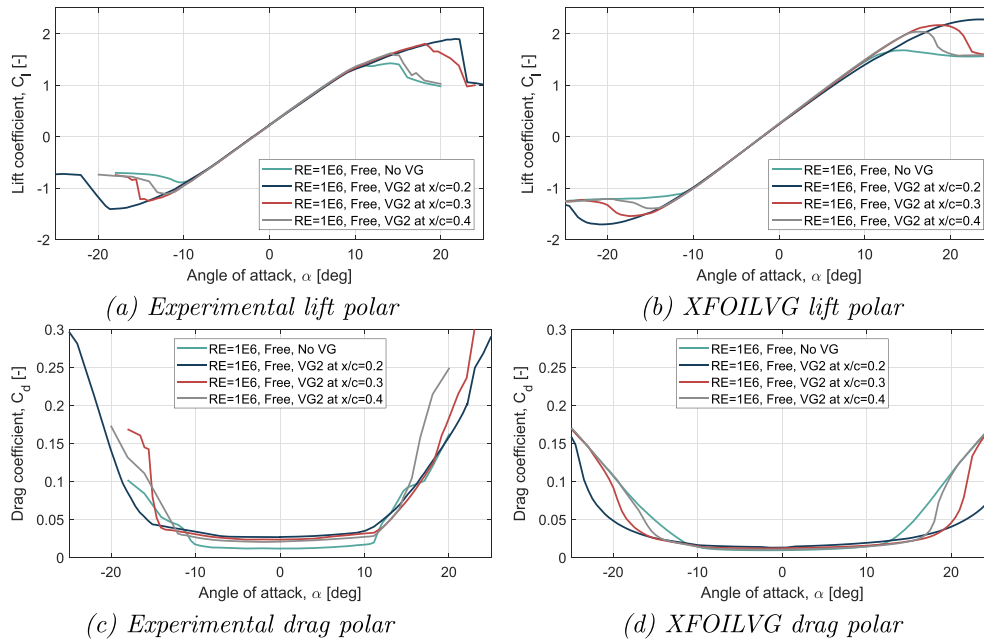


Figure A.20. Experimental lift and drag polar and polars obtained with XFOILVG [52] in free transition with various VG2 configurations.

Table A.2

Airfoil coordinates of DU17DBD25 airfoil.

$x/c [-]$	$y/c [-]$
1	0.0068
0.966454	0.013244
0.902653	0.025238
0.830271	0.039774
0.755865	0.056557
0.679287	0.075557
0.601612	0.095573
0.528128	0.11365
0.460557	0.128092
0.398278	0.138356
0.340473	0.144181
0.286646	0.145743
0.236802	0.143136
0.19145	0.136855
0.151288	0.127557
0.116954	0.116197
0.088506	0.103715
0.065522	0.090921
0.047262	0.07823
0.032911	0.065847
0.021793	0.053847
0.013382	0.042264
0.007304	0.031114
0.003205	0.020469
0.000819	0.010404
-8E-06	0.000978
0.000967	-0.00828
0.004465	-0.01758
0.010525	-0.02662
0.018979	-0.0354
0.02993	-0.0441
0.043797	-0.05292
0.061335	-0.06209
0.083657	-0.07174
0.112205	-0.08173
0.14815	-0.0916
0.191479	-0.10023
0.241028	-0.10632
0.295108	-0.109
0.352739	-0.10772
0.413882	-0.10244
0.478977	-0.09311

Table A.2 (continued)

$x/c [-]$	$y/c [-]$
0.548989	-0.08001
0.624481	-0.06385
0.701668	-0.047
0.774889	-0.03235
0.843826	-0.0209
0.908437	-0.013
0.966823	-0.00838
1	-0.0068

References

- [1] D. Baldacchino, Vortex Generators for Flow Separation Control Wind Turbine Applications, Phd thesis, Delft University of Technology, 2019, <https://doi.org/10.4233/uuid:99b15acb-e25e-4cd9-8541-1e4056c1baed>.
- [2] C. P. Butterfield, Aerodynamic pressure and flow-visualization measurement from a rotating wind turbine blade, Proceedings of the Eighth ASME Wind Energy Symposium.
- [3] D. E. Shipley, M. M. S. R. M. C, Dynamic stall occurrence on a horizontal axis wind turbine blade, Proceedings of 14th ASME-ETCE Wind Energy Symposium (NREL/TP-442-6912).
- [4] A. Choudhry, M. Arjomandi, R. Kelso, Horizontal axis wind turbine dynamic stall predictions based on wind speed and direction variability, Proc. IME J. Power Energy 227 (3) (2013) 338–351.
- [5] J.G. Leishman, Challenges in modelling the unsteady aerodynamics of wind turbines, Wind Energy 5 (2–3) (2002) 85–132.
- [6] K.M. Arsalan, Dynamic Stall Modeling for Wind Turbines, Msc thesis, Delft University of Technology, 2018.
- [7] C.S. Ferreira, The Near Wake of the VAWT, Phd thesis, Delft University of Technology, 2009.
- [8] C.S. Ferreira, G. Van Kuik, G. Van Bussel, F. Scarano, Visualization by PIV of dynamic stall on a vertical axis wind turbine, Exp. Fluid 46 (1) (2009) 97–108.
- [9] C. Ferreira, G. van Bussel, F. Scarano, G. van Kuik, PIV visualization of dynamic stall VAWT and blade load determination, Proceedings of 46th AIAA Aerospace Sciences Meeting and Exhibit.
- [10] A. Allet, I. Paraschivoiu, Viscous flow and dynamic stall effects on vertical-axis wind turbines, Int. J. Rotating Mach. 2 (1) (1995) 1–14.
- [11] A.J. Buchner, M.W. Lohry, L. Martinelli, J. Soria, A.J. Smits, Dynamic stall in

- vertical axis wind turbines: comparing experiments and computations, *J. Wind Eng. Ind. Aerod.* 146 (2015) 163–171.
- [12] E. Dyachuk, A. Goude, Simulating dynamic stall effects for vertical axis wind turbines applying a double multiple streamtube model, *Energies* 8 (2) (2015) 1353–1372.
- [13] C.J.S. Ferreira, A. van Zuijlen, H. Bijl, G. van Bussel, G. van Kuik, Simulating dynamic stall in a two-dimensional vertical-axis wind turbine: verification and validation with particle image velocimetry data, *Wind Energy* 13 (1) (2010) 1–17.
- [14] A. Zanon, P. Giannattasio, C.J. Simo Ferreira, Wake modelling of a VAWT in dynamic stall: impact on the prediction of flow and induction fields, *Wind Energy* 18 (11) (2015) 1855–1874.
- [15] A. Choudhry, M. Arjomandi, R. Kelso, Methods to control dynamic stall for wind turbine applications, *Renew. Energy* 86 (2016) 26–37.
- [16] W. J. McCroskey, K. W. McAlister, L. W. Carr, S. L. Pucci, O. Lambert, Dynamic stall on advanced airfoil sections, Proceedings of 36th Annual Forum of the American Helicopter Society.
- [17] W. J. McCroskey, reportLecture Notes on the Phenomenon of Dynamic Stall, Report NASA Technical Memorandum 81264, National Aeronautics and Space Administration.
- [18] L.W. Carr, Progress in analysis and prediction of dynamic stall, *J. Aircraft* 25 (1) (1988) 6–17.
- [19] T. Theodorsen, General Theory of Aerodynamic Instability and the Mechanism of Flutter, Report, NASA, 1935.
- [20] G. B. Schubauer, W. G. Spangenberg, Forced mixing in boundary layers, *J. Fluid Mech.* 8 (01).
- [21] D. Baldacchino, M. Manolesos, C. Ferreira, A. Gonzalez Salcedo, M. Aparicio, T. Chaviaropoulos, K. Diakakis, L. Florentie, N. Garcia, G. Papadakis, Experimental benchmark and code validation for airfoils equipped with passive vortex generators, *J. Phys. Conf.* 753 (2) (2016), 022002.
- [22] D. Baldacchino, C. Ferreira, D. De Tavernier, W.A. Timmer, G.J.W. van Bussel, Experimental parameter study for passive vortex generators on a 30% thick airfoil, *Wind Energy* 21 (9) (2018) 745–765.
- [23] P. Martin, J. Wilson, J. Berry, T. Wong, M. Moulton, M. McVeigh, Passive control of compressible dynamic stall, Proceedings of 26th AIAA Applied Aerodynamics Conference.
- [24] W. Geissler, G. Dietz, H. Mai, Dynamic Stall and its Passive Control Investigations on the OA209 Airfoil Section, European Rotorcraft Forum.
- [25] B. Heine, K. Mulleners, G. Joubert, M. Raffel, Dynamic stall control by passive disturbance generators, *AIAA J.* 51 (9) (2013) 2086–2097.
- [26] A.L. Pape, M. Costes, F. Richez, G. Joubert, F. David, J.M. Deluc, Dynamic stall control using deployable leading-edge vortex generators, *AIAA J.* 50 (10) (2012) 2135–2145.
- [27] C. Zhu, T. Wang, J. Wu, Numerical investigation of passive vortex generators on a wind turbine airfoil undergoing pitch oscillations, *Energies* 12 (4).
- [28] C. Zhu, J. Chen, J. Wu, T. Wang, Dynamic stall control of the wind turbine airfoil via single-row and double-row passive vortex generators, *Energy* 189.
- [29] A.D. Gardner, K. Richter, H. Rosemann, Numerical investigation of air jets for dynamic stall control on the OA209 airfoil, *CEAS Aeronautical Journal* 1 (1–4) (2011) 69–82.
- [30] H. Mueller-Vahl, C. Strangfeld, C.N. Nayeri, C.O. Paschereit, D. Greenblatt, Thick airfoil deep dynamic stall using static blowing, *Research Topics in Wind Energy* (2014) 35–40, https://doi.org/10.1007/978-3-642-54696-9_6, book section (Chapter 6).
- [31] H.F. Müller-Vahl, C.N. Nayeri, C.O. Paschereit, D. Greenblatt, Dynamic stall control via adaptive blowing, *Renew. Energy* 97 (2016) 47–64.
- [32] D. Greenblatt, I. Wygnanski, Dynamic stall control by periodic excitation, Part 1: NACA 0015 parametric study, *J. Aircraft* 38 (3) (2001) 430–438.
- [33] D. Greenblatt, B. Nishri, A. Darabi, I. Wygnanski, Dynamic stall control by periodic excitation, Part 2: Mechanisms, *J. Aircraft* 38 (3) (2001) 439–447.
- [34] D. Velasco, O.L. Mejia, S. Lain, Numerical simulations of active flow control with synthetic jets in a Darrieus turbine, *Renew. Energy* 113 (2017) 129–140.
- [35] M. A. Karim, A. M. Suppression of dynamic-stall vortices over pitching airfoils by leading-edge suction, *AIAA J.* 32 (8).
- [36] D. Greenblatt, A. Ben-Harav, M. Schulman, Dynamic Stall Control on a Vertical axis Wind Turbine Using Plasma Actuators, 2012.
- [37] M. L. Post, T. C. Corke, Separation control using plasma actuators: dynamic stall vortex control on oscillating airfoil, *AIAA J.* 44 (12).
- [38] D. Greenblatt, R. Lautman, Inboard/outboard plasma actuation on a vertical-axis wind turbine, *Renew. Energy* 83 (2015) 1147–1156.
- [39] D. Greenblatt, M. Schulman, A. Ben-Harav, Vertical axis wind turbine performance enhancement using plasma actuators, *Renew. Energy* 37 (1) (2012) 345–354.
- [40] Delft University of Technology, Low Turbulence Tunnel (LTT), 2017. <https://www.tudelft.nl>. (Accessed 8 September 2017).
- [41] Unimotion, CAD Drawings Linear Actuator and Accessories, 2020. <https://unimotion.eu/>. (Accessed 1 April 2020).
- [42] Tulip Wind, A Dutch IMBY Approach to Renewable Energy, Topsector Energie, 2017. <https://projecten.topsectorenergie.nl/projecten/tulip-wind-a-dutch-imby-approach-to-renewable-energy-00031379>. (Accessed 13 July 2020).
- [43] C.S. Ferreira, B. Geurts, Aerofoil optimization for vertical-axis wind turbines, *Wind Energy* 18 (8) (2015) 1371–1385.
- [44] C. S. Ferreira, M. F. Barone, A. Zanon, R. Kemp, P. Giannattasio, Airfoil optimization for stall regulated vertical axis wind turbines, AIAA SciTech Forum: 33rd Wind Energy Symposium (2015-0722).
- [45] D. Ragni, C.S. Ferreira, G. Correale, Experimental investigation of an optimized airfoil for vertical-axis wind turbines, *Wind Energy* 18 (9) (2015) 1629–1643.
- [46] D. De Tavernier, C. Ferreira, G. Bussel, Airfoil optimisation for vertical axis wind turbines with variable pitch, *Wind Energy* 22 (4) (2019) 547–562.
- [47] M. Drela, H. Youngren, Xfoil 6.9 User Primer, 2001. http://web.mit.edu/drela/Public/web/xfoil/xfoil_doc.txt. (Accessed 29 February 2016).
- [48] C. Dalton, Allen and Vincenti blockage correction in a wind tunnel, *AIAA J.* 9 (9) (1971) 1864.
- [49] J.C. Alves, S. Tirtzy, S. Paris, Premesys v2.0, a Software Tool to Characterize the Dynamic Response of a Pressure Measurement System, Report, Von Karman Institute for Fluid Dynamics, 2015.
- [50] H. Bergh, H. Tjeldeman, Theoretical and Experimental Results for the Dynamic Response of Pressure Measuring Systems, Report NLR-TR F.238, National Aero- and astronomical research institute Amsterdam, 1965.
- [51] D. De Tavernier, C. Ferreira, Experimental Data: Experimental Study on Dynamic Stall Control Using Vortex Generators, 4TU Research Data, 2020, <https://doi.org/10.4121/13089581>.
- [52] D. De Tavernier, D. Baldacchino, C. Ferreira, An integral boundary layer engineering model for vortex generators implemented in XFOIL, *Wind Energy* 21 (10) (2018) 906–921.
- [53] J.G. Leishman, Dynamic stall experiments on the NACA23012 aerofoil, *Exp. Fluid* 9 (1990) 49–58.
- [54] T.T. Rice, K. Taylor, M. Amitay, Wind tunnel quantification of dynamic stall on an S817 airfoil and its control using synthetic jet actuators, *Wind Energy* 22 (1) (2019) 21–33.
- [55] J.M. Yu, T.S. Leu, J.J. Miao, Investigation of reduced frequency and freestream turbulence effects on dynamic stall of a pitching airfoil, *J. Visual* 20 (1) (2016) 31–44.
- [56] K.K.Y. Tsang, R.M.C. So, R.C.K. Leung, X.Q. Wang, Dynamic stall behavior from unsteady force measurements, *J. Fluid Struct.* 24 (1) (2008) 129–150.
- [57] X. Liu, S. Liang, G. Li, Godbole, C. Lu, An improved dynamic stall model and its effect on wind turbine fatigue load prediction, *Renew. Energy* 156 (2020) 117–130.

Nomenclature

- α : Angle of attack [°]
 α_0 : Mean angle of attack in oscillations [°]
 β_{VG} : Inflow angle of vortex generators [°]
 μ : Dynamic fluid viscosity [Pas]
 ρ_s : Mean air density [kg/m^3]
 A : Oscillation amplitude [°]
 c : Airfoil chord length [m]
 C_n' : 2D normal coefficient (uncorrected) [–]
 $C_{m,LE}'$: 2D moment coefficient around leading edge (uncorrected) [–]
 C_d' : 2D drag coefficient (corrected) [–]
 C_l' : 2D lift coefficient (corrected) [–]
 C_m : 2D moment coefficient around quarter-chord point (corrected) [–]
 $C_{m,LE}$: 2D moment coefficient around leading edge (corrected) [–]
 $C_{p,l}$: Pressure coefficient lower surface [–]
 $C_{p,s}$: Static pressure coefficient [–]
 $C_{p,t}$: Total pressure coefficient [–]
 $C_{p,u}$: Pressure coefficient upper surface [–]
 D_{VG} : External pair distance of vortex generators [mm]
 d_{VG} : Internal pair distance of vortex generators [mm]
 f : Oscillation frequency [Hz]
 h_{VG} : Height of vortex generators [mm]
 k : Reduced frequency [–]
 L : Pressure tube length [m]
 l_{VG} : Length of vortex generators [mm]
 p : Pressure [Pa]
 Pr : Prandtl number [–]
 R : Pressure tube radius [m]
 RE : Reynolds number [–]
 t : Time [s]
 V_∞ : Incoming velocity [m/s]
 V_t : Tube volume [m^3]
 V_v : Transducer volume [m^3]
 x : X-coordinate airfoil profile, chordwise position [m]
 y : Y-coordinate airfoil profile [m]